https://doi.org/10.5194/bg-2023-62
Preprint. Discussion started: 13 April 2023

Biogeosciences Discussions
Open Access
EGU

Down in the dungeons: microbial redox reactions and geochemical transformations define the biogeochemistry of an estuarine sediment column

Thibault Duteil[1], Raphaël Bourillot[1], Olivier Braissant[2], Adrien Henry[1], Michel Franceschi[1], Marie-Joelle Olivier[1], Nathalie Le Roy[1], Benjamin Brigaud[3], Eric Portier[4] & Pieter T. Visscher[5,6]

[1] Univ. Bordeaux, CNRS, Bordeaux INP, EPOC, UMR 5805, 33600 Pessac, France
[2] Center for Biomechanics and Biocalorimetry, University of Basel, c/o Department Biomedical Engineering (DBE), Hegenheimermattweg 167C, Allschwil 4123, Switzerland
[3] Université Paris-Saclay, CNRS, GEOPS, 91405 Orsay, France
[4]45-8 Energy, 4, rue François de Curel, 57000 Metz, France
[5] Department of Marine Sciences and Geosciences, University of Connecticut, Groton, Connecticut 06340, USA
[6] Université de Bourgogne Franche-Comté, CNRS, Biogéosciences, 21000 Dijon, France

Correspondence to: Thibault Duteil (duteilthibault@gmail.com)

Abstract

The surface of intertidal estuarine sediments is typically covered with a photosynthetic biofilm. A large fraction of the carbon that is fixed is in the form of exopolymeric substances (EPS), providing the biofilm matrix. The consumption of organic carbon within the sediment column by heterotrophs bacteria is stratified according to the availability of electron acceptors used for organic matter degradation. This sequential use of electron acceptors strongly impacts geochemical gradients and early diagenetic processes within the sediment. In most studies, the distribution and role of the predominant microbial metabolisms is deduced from porewater chemistry and restricted to the upper decimeters of the sediment column, but rarely from direct measurements of microbial activity, potentially leading to erroneous conclusions of biogeochemical processes.

We measured geochemical gradients in three estuarine sediment cores to a depth of 6 meters. Geochemical analyses of porewater and sediment were combined with measurements of microbial activity. In situ microelectrode measurements were performed for pH, oxygen and sulfide. Porewater was extracted and analyzed for major elements using Ion Chromatography, Inductively-Coupled-Plasma, and colorimetric assays for iron speciation. Porewater chemistry was compared to measurements of microbial activity including isothermal

https://doi.org/10.5194/bg-2023-62
Preprint. Discussion started: 13 April 2023

calorimetry and metabolic assays (triphenyltetrazolium chloride (TTC) and fluorescein diacetate (FDA)) and concentrations of EPS (sugars, proteins) measured in a previous study on the same cores. Finally, sediment composition was characterized through X-Ray Fluorescence core scanning.

Results show that: (i) aerobic respiration occurred between 0 and 1 cm, (ii) nitrate reduction between 6 and 16 cm, (iii) sulfate reduction between 10 and 50 cm, (iv) manganese oxide reduction between 2-6 and 35-50 cm and (v) iron oxide reduction between 16-18, 24-26 and 35-45 cm. This is concomitant with the area where the microbial activity is the highest. In contrast to the literature, we conclude that some reactions, for example sulfate and nitrate reduction, were locally coupled or at least occurred concomitantly.

Impacts of microbial metabolism on early diagenesis have been modeled via PhreeQc and predicted potential precipitation of metastable iron and/or sulfides. This is confirmed by iron and sulfur increases in sediments characterized through XRF. All these observations have been used to propose a biogeochemical model linking microbial metabolisms and early diagenesis that can be used as a basis for the study of other geochemical profiles in the future.

Introduction

Estuaries are transition zones at the interface of continental and oceanic environments with specific geochemical cycles (Chiffoleau et al., 1994; Kraepiel et al., 1997; Stecko & Bendell-Young, 2000). Estuarine mixing of seawater and freshwater leads to change in metal ligands (e.g., organic versus chlorine), increased metal release and cycling in the sediments, and estuaries are important sinks for many persistent pollutants and their subsequent accumulation (de Souza Machado et al., 2016; Schäfer et al., 2022). Fine-grained sediments, such as silt and clay, are especially prone to trace metal accumulation because of their high adsorption properties (Chatterjee et al., 2007).

Sediment-associated biofilms are particularly efficient in the cycling of key elements, e.g., C, N, S, Fe. The cycling of elements by microorganisms results in coupled reactions of oxidation and reduction, producing steep vertical geochemical gradients (e.g., dissolved oxygen, pH) that influence metal speciation in the sediment (Visscher & Stolz, 2005). Photoautotrophic benthic biofilms typically develop at the water-sediment interface (Underwood & Paterson, 2003; De Winder et al., 1999). In estuarine intertidal zones, these biofilms are often dominated by diatoms, and could be responsible for up to 50% of the autotrophic production (Underwood & Kromkamp, 1999). Diatom biofilms perform oxygenic photosynthesis during daylight, in the process producing oxygen (Glud et al., 1992) and organic carbon, including exopolymeric substances (EPS; Decho, 2000; Underwood & Paterson, 2003).

https://doi.org/10.5194/bg-2023-62
Preprint. Discussion started: 13 April 2023

The organic carbon produced by photoautotrophs can be consumed and reoxidized to CO_2 by heterotrophs through various respiratory and fermentative pathways. Heterotrophs are generally stratified according to a gradient of electron acceptors with decreasing free energy yield: oxygen, nitrate, manganese and iron oxides, sulfate and methane (Sagemann et al., 1996; Megonigal et al., 2003; Visscher & Stolz, 2005; Konhauser, 2009). Aerobic respiration results in an almost complete consumption of oxygen at shallow depth in the sediment (i.e., millimeters to centimeters; Sagemann et al., 1996; Megonigal et al. 2003; Jørgensen & Nelson, 2004; Hensen et al., 2006). The subsequent formation of anoxic microenvironments allows the predominance of anaerobic heterotrophs performing denitrification and sulfate reduction (Burdige & Zheng, 2003; Jorgensen & Nelson, 2004; Mortimer et al., 2004; Audry et al., 2006). Due to their sensitivity to redox conditions, dissolved iron and manganese profiles typically show more complex patterns. For example, in the oxic zone, Fe(II) oxidation by iron oxidizing bacteria can result in ferrihydrite precipitation in Fe(II) and Fe(III)-rich environments (Mc Allister et al., 2015). In the anoxic zone, the mineralization of organic carbon coupled with the reduction and solubilization of solid Mn (III/IV) and Fe (III) species could result from both chemical and microbial reactions (Tugel et al., 1986; Burdige, 2011). This reduction often coincides with sulfate and sulfur respiration (Sundby et al., 1986; Burdige, 1993; Canfield et al., 1993; Fiket et al., 2019) and leads to the precipitation of reduced manganese and iron phases, such as sulfides (e.g., mackinawite, pyrite; Sorensen & Jorgensen, 1987). When preserved from oxidation, these mineral phases can be considered as mineral markers of reducing porewaters in ancient sedimentary rocks (Marin Carbonne et al., 2014). Although absent in the first centimeters of sediments, iron reduction generally occurs in the upper few decimeters of the sediments and ferrous iron cation (Fe^{2+}) concentration increases with depth (Sorensen & Jorgensen, 1987; Burdige, 1993; Canfield et al., 1993). Finally, when sulfate is depleted methanogenesis becomes the predominant metabolism for the mineralization of organic carbon in tidal flat sediments (Megonigal et al. 2003; Webster et al., 2010; O'Sullivan et al., 2013).

Through their combined metabolic activity, microorganisms modify the concentration profiles of these electron acceptors, but also indirectly of other elements such as trace metals. For example, cadmium can be released in estuarine pore water through organic matter degradation associated with Mn and Fe reduction (Audry et al., 2005). This general model of microbial stratification may vary depending on microbial communities or environmental conditions (Visscher & Stolz, 2005). For example, sulfate reduction or methanogenesis can be active in the zone of oxygenic photosynthesis of microbial mats (Visscher et al., 1991; Pace et al., 2018). Coupled reduction reactions or overlap of these have been documented; for example, denitrification and manganese reduction may co-occur due to close ΔG^o values (Klinkhammer et al., 1980; Burdige, 1993). These models are also locally complexified

https://doi.org/10.5194/bg-2023-62
Preprint. Discussion started: 13 April 2023

by hydrological and sedimentary properties such as surface or groundwater flow, and sedimentary architecture (McAllister et al., 2015; Beck et al., 2017). For instance, low river discharge can enhance carbon remineralization in estuaries by displacing the salinity gradient upstream (Meiggs & Taillefert, 2011).

Many previous studies discussed the potential links between microbial metabolisms and early diagenesis, but only to depths of around 20 cm (Burdige & Gieskes, 1983; Sorensen & Jorgensen, 1987; Hensen et al., 2006). In the Gironde estuary, gradients of several elements (O_2, NO_3^-, SO_4^-, Fe, Mn) were studied from the water column down in the sediments to 50 cm depth (Audry et al., 2006), but these studies did not include direct measurements of metabolic activities and the role of microbes was only assumed. To date, no study has combined sediment, porewater chemistry and microbial activity to characterize early diagenetic geomicrobiological processes in estuarine sediments.

In the current study, we investigated the relationships between microbial activity and the cycling of major elements in estuarine sediments. Two sediment cores and one box core were collected in an estuarine point bar from the Gironde Estuary (southwest France). The changes in microbial activities with depth was measured with metabolic assays (microbially active cells and hydrolytic activity) coupled to microcalorimetry. Microelectrode measurements of O_2, pH and HS^-, were combined with porewater concentrations of SO_4^{2-}, NO_3^-, Fe (II/III), Mn^{2+}, Ca^{2+}, Mg^{2+}, Na^+, Cl^- measured by Ion Chromatography and Inductively Coupled Plasma atomic emission spectroscopy. The potential for metal dissolution and precipitation was evaluated based on core-scale X-Ray Fluorescence and porewater geochemical modeling. Following statistical analyses of this dataset, we finally propose an integrative model of estuarine sediment geomicrobiology that includes early diagenesis.

Materials and Methods

Field site description, sample location, and core sampling

Field campaigns were held at the Bordeaux North point bar, located in the Garonne estuarine channel, in June 2019. A 6.23 m long vertical core (BXN Long Core or BXN-LC; 44°53'47.40"N, 0°32'24.80"W; Figure 1A) was extracted from the chute channel with a portable vibro-corer (see Duteil et al., 2022 for more sedimentary details about BXN-LC). In order to preserve sediment structures from deformation and fluidization due to water escape, the core barrel is hammered without any rotation and the piston is maintained with a cable. A second, 0.7 m long core (BXN Short Core or BXN-SC; 44°53'45.00"N, 0°32'23.40"W; Figure 1) was extracted with a hand-held core sampler. Finally, a sediment box core (BXN box or BXN-B; 44°53'45.00"N, 0°32'23.40"W; Figure 1) was sampled

https://doi.org/10.5194/bg-2023-62
Preprint. Discussion started: 13 April 2023

in the same area with a steel sampling box (length: 30cm, width: 17.5cm, depth: 6.2cm). After removal from the sediment, the cores were sealed and kept vertical to avoid water mixing and stored at 4°C until analyzed.

Porewater chemistry: microelectrode measurements

Porewater dissolved oxygen (O_2) concentrations were measured in the field down to a depth of 1.4 cm with a vertical resolution of 250 µm using a polarographic microelectrode. Subsequently, the concentrations of O_2, sulfide (H_2S/S^{2-}), and pH were measured in the laboratory by inserting microelectrodes in the sediment through holes in the core tubing (vertical resolution: 0.2 mm). The measurements for O_2, H_2S/S^{2-} and pH were taken using polarographic and ion-specific needle microelectrodes in combination with a field microsensor multimeter (Unisense, Aarhus, Denmark; Visscher et al., 2000) and measurements for S^{2-} using a high-impedance millivolt meter (Microscale Measurements, The Hague, The Netherlands). The [HS^-] was calculated by combining H_2S or S_2^- readings with pH measurements at each depth (Visscher et al., 1991). Detection limits for electrode measurements were better than one µM for O_2, and better than five µM for H_2S, and two µM for the S^{2-} electrode. Depth profiles were determined three times for each analyte. The temperature and conductivity of the overlying water were measured with an Accumet AP-75 handheld meter and pH using a Mettler Toledo GoFive meter.

Porewater chemistry: water extraction

Porewater was sampled with rhizons (pore diameter of 0.1 µm; Rhizosphere Research Products; Wageningen) inserted in holes drilled in the core tubings. A total of 34 pore water samples were extracted, 12 for BXN-B (*ca.* 1 sample every 5 cm), 6 for BXN-SC (ca. one sample every 12 cm) and 16 for BXN-LC (*ca*. 1 sample every 40 cm). In order to improve water recovery, rhizons were saturated with deionized water for 30 minutes before use. 25 mL syringes were connected with the Luer-Lock system to the rhizons with a wooden retainer to create a vacuum. Water sampling was performed over 24 hours, then syringes were closed with Luer-Lock plugs and stored in the fridge (4°C) until processing.

Porewater chemistry: major dissolved elements measurements and modeling

Major cation (Ca^{2+}, Mg^{2+}, Mn^{2+}, Na^+, K^+) and anion (Cl^-, NO_3^-, and PO_4^{3-}) concentrations were determined by ion chromatography (IC; Dionex ICS-1500) in the 34 porewater samples, with an analytical precision of 0.2 $mg.L^{-1}$. Metal concentrations (Cd^{2+}, Ca^{2+}, Mg^{2+}, dissolved Mn, dissolved Fe, Pb^{2+}, Zn^{2+}) were measured by ICP-OES (in the same samples) at Eurofins laboratory (Bordeaux) with an analytical precision of 0.1 $mg.L^{-1}$. Two depth

https://doi.org/10.5194/bg-2023-62
Preprint. Discussion started: 13 April 2023

intervals did not yield enough water for analyses, and five did not allow enough water for ICP measurements from BXN-B and BXN-SC (Table S1). Iron speciation (Fe(II)/Fe(III)) was determined on 16 samples from BXN-LC using the 1,10-phenantroline colorimetric test (ref LCK 321; Hach Lange) with a Hach DR 3900 spectrophotometer (Hach Lange, CO, USA). The concentrations were entered in the geochemical modeling software Phreeqc to determine the saturation index of oxides, sulfides and carbonates using the Pitzer model (Pitzer, 1979).

Core opening, processing and sampling

Upon opening, the cores were immediately photographed. Two-dimensional X-ray images of the cores were obtained with a SCOPIX device (EPOC laboratory, Bordeaux; Migeon et al., 1998), allowing for identification of sedimentary fabrics with a non-destructive approach at high resolution (125 µm). Core sedimentology was subsequently analyzed in order to identify the main facies changes. For metabolic assays 2 g of sediment were taken in 9 samples from the BXN-BOX (one cm interval between 0-5 cm, then 5 cm), 6 from the BXN-SC (*ca*. one sample every 6 cm) and 16 from the BXN-LC (*ca*. one sample every 40 cm). X-ray fluorescence spectrometric analysis (XRF) was carried out on the archive halves of BXN-SC and BXN-LC with a XRF core scanner (AVAATECH XRF Core Scanner; Avaatech; Netherlands).

Metabolic assays

The triphenyltetrazolium chloride (TTC) assay was used as a proxy for metabolically active cells in the sediment. The total reductase activity was measured in 34 samples (in triplicates) through the reduction of TTC to triphenylformazan in order to identify cells that exhibit metabolic activity (Relexans, 1996; Braissant et al., 2020). For this, 2 g of sediment were homogenized and mixed with 2 mL of 0.8% TTC in Instant Ocean adjusted to estuarine water (pH 7.1; salinity 1 $g.L^{-1}$) to obtain a final concentration of 0.4% TTC. The samples were incubated for 3 h at 30°C. Following the incubation, the samples were centrifuged (3000 x g, 10 min) and the pellet was resuspended in 4 mL of acetone to extract the triphenylformazan. After 5 minutes, the sample was centrifuged (3000 x g, 3 min) and the absorbance of the supernatant at 490 nm was measured with a spectrophotometer (Helios Epsilon, Thermo Fisher Scientific). The concentration of formazan was calculated with the Beer-Lambert law with a molar absorption coefficient of 14 320 $L.mol^{-1}.cm^{-1}$. Blanks were prepared by adding 2 mL of 1.5% glutaraldehyde to the sediment. Active diatom cells were used as a positive control (Figure S1).

https://doi.org/10.5194/bg-2023-62
Preprint. Discussion started: 13 April 2023

The fluorescein diacetate (FDA) assay was used as a proxy for the hydrolytic activity in the sediment. The hydrolytic activity of the ubiquitous lipase, protease, and esterase enzymes (non-specific hydrolases) was measured in 34 samples (in triplicates) by the hydrolysis of the FDA into fluorescein (Green et al., 2006; Braissant et al., 2020). For this, 2 g of sediment were homogenized in 4 mL of Instant Ocean adjusted to estuarine water (pH 7.1; salinity 1 $g.L^{-1}$) and 60 µL of FDA solution (1 $mg.mL^{-1}$ in acetone). The samples were incubated for 24 h at 30°C. Following incubation, the fluorescein was extracted by adding 4 mL of acetone. After five minutes, the sample was centrifuged (3000 x g, 3 min) and the absorbance of the supernatant was measured at 490 nm with a spectrophotometer (Helios Epsilon, Thermo Fisher Scientific). The concentration of fluorescein was calculated with the Beer-Lambert law considering a molar absorption coefficient of 73,350 $L.mol^{-1}.cm^{-1}$. Blanks were prepared by adding 2 mL of 1.5% glutaraldehyde to the sediment. Active diatom cells were used as a positive control (Figure S1).

Isothermal calorimetry (IMC)

Isothermal calorimetry had proven to be very useful to directly assess bacterial activities without having to culture the organisms separately (Braissant et al., 2012). For example, observations of benthic marine sediments showed that there was a linear relationship between the dehydrogenase activity assayed using TTC and heat production (Pamatmat et al., 1981). For IMC measures, 2 g of sediments were incubated in a TAM Air calorimeter (TA Instruments, New Castle, DE) with 200 µL of R2A culture medium (Reasoner & Geldreich, 1985). Autoclaved (20 min; 121°C) sediment samples were used as a blank. For each depth, sampling was carried out in triplicate. The heat release was measured during 24 h to quantify the microbial activity. The specific growth rate (µ), the lag phase (λ) and the heat produced (Q) were calculated by fitting the heat-over-time curve with the modified Gompertz model (Gil et al., 2006; Braissant et al., 2012). The growth rate (µ) predicts how fast the bacterial community could grow using the experimental substrate (h). The lag time (λ) corresponds to the time before the bacterial community shows activity. The maximum heat flow was used to estimate the number of active cells, assuming a heat production rate of 3 $pW.cell^{-1}$. For aerobic microbial plate counts, 1 g of sample was dissolved in 10 mL of PBS then subjected to 10 folds dilution series. The appropriate dilutions were then poured into a petri dish containing R2A medium and 1.5% agar. Colonies were counted after 1 (CFU 1), 7 (CFU 7) and 30 (CFU 30) days and aerobic microbial numbers were calculated using the sample dilutions.

Statistical analyses

https://doi.org/10.5194/bg-2023-62
Preprint. Discussion started: 13 April 2023

All the statistical analyses were performed using the R software (R Core Team, 2013). PCA were achieved using the *prcomp* function and visualized with the factoextra package and *fviz pca* function. Correlation matrices were calculated with the *cor function* and visualized with the package Corrplot. Finally, the *rcorr* function of the package Hmisc was used to calculate the level of significance for the Pearson and Spearman correlations.

Results

BXN-B and BXN-SC were sampled in close proximity (5 cm). As they show a very similar sedimentary succession, and in order to simplify the results, BXN-B and BXN-SC were grouped together in the results. All data are available as part of the supplementary material (Tables S1 and S2).

Sedimentary description

The BXN-B and BXN-SC are dominated by two sedimentary facies: facies F2 tidal sand dunes and facies F3 heterolithic fine sands and laminated mud (see Duteil et al., 2022 for a detailed facies description). Ebb-oriented sand dunes (F2) were found between 72 and 30 cm, with dune foresets locally draped by muds forming mud couplets (Figure 1). Mud pebbles are abundant between 56 and 42 cm. This is followed by silty heterolithic deposits (F3) between 30 and 20 cm alternating with sands dunes. A second ebb-oriented sand dune interval (F2) similar to the first one was observed between 20 and 0 cm (Figure 1). The average grain size of sediments is 274 µm with an average grain composition of quartz (39%), silt-clays (25%), lithics (e.g. wood debris; 5%), micas (2%), other grains (3%) and feldspars (1%).

Porewater analysis

In BXN-B and BXN-SC, the concentration of dissolved oxygen (O_2) increased from 223 to 476 µM between 0 and 3 mm depth, and decreased exponentially to 5 µM at 13 mm depth (Figure 2). The O_2 concentration remained very low between 2 and 30 cm (between 0.25 and 11 µM), and reached 0 at 35 centimeters. In the same core, pH increased from 7.9 to 8.2 between 0 and 12 cm depth, and stabilized around 8.2 below 12 cm (Figure 2).

Sulfide concentrations (HS^-) were not considered at the top and the bottom of the cores BXN-B and BXN-SC (0, 26 and 65 cm deep), because of the potential of oxygen diffusion following sampling. [HS^-] was not detected in the upper two cm after which it increased to 240 µM at 20 cm depth (Figure 2). This was followed by a decrease to 157 µM at 24 cm, after which it remained relatively constant (152-163 µM) down to 40 cm and decreased further to 129 µM at 50 cm, before finally increasing to 165 µM at 60 cm.

https://doi.org/10.5194/bg-2023-62
Preprint. Discussion started: 13 April 2023

The sulfate concentration (SO_4^{2-}) was 87.3 µM at two cm below the sediment surface and decreased to 50.8 µM (Figure 2) at 6 cm. [SO_4^{2-}] increased to 96.2 µM at 12 cm and reached zero at 18 cm. At 20 cm, the concentration increased again to 20.8 µM, and was low between 22 and 26 cm (0-73 µM). The concentration increased to 81.2 µM at 30 cm, rapidly decreased to 2.5 µM at 35 cm, after which it rose again to 61.4 µM at 40 cm. [SO_4^{2-}], and remained low, around 0-1 µM between 50 and 65 cm. In BXN-LC, sulfate concentration was at 5.7 µM at 60 cm, and decreased to approximately 1.56 µM between 50 cm and 130 cm (Figure 3). The sulfate concentration then increased to 10.8 µM between 130 and 160 cm. Sulfate was not detected between 216 and 259 cm, and concentrations remained low below 280 cm (0-3 µM), except at 325 cm (5.8 µM).

Nitrate was absent between 0 and 6 cm, after which the concentration increased to 98.3 µM at eight cm (Figure 2). The [NO_3^-] dropped to 29.4 µM at 10 cm and increased to 45.8 µM at 12 cm. [NO_3^-] fell to 0 µM at 16 cm and remained below the detection limit until 65 cm depth. In BXN-LC, the concentration rose from 16.4 to 22.4 µM between 6 and 50 cm depth (Figure 3). The nitrate concentration decreased to 0 at 163 cm and remained absent down to 259 cm depth. Low nitrate concentrations of 2.3 and 2.7 µM were found at 280 and 325 cm before decreasing to 0 near the bottom of the core.

In BXN-B and BXN-SC, no dissolved iron (Fe) was present from the sediment surface down to 10 cm depth. Iron concentrations reached 2.7 µM at 18 cm before decreasing to zero at 24 cm depth (Figure 2). Iron concentration reached 2.5 µM at 26 cm before decreasing to 0.07 µM at 35 cm. The concentration went up to 1.2 µM at 50 cm before reaching 0 at 65 cm. Concentrations were below the detection limit of the assay in BXN-B and BXN-SC.

The concentrations of dissolved iron species, Fe(II) and Fe(III), were measured in BXN-LC (Figure 3). Fe(II) and Fe(III) increased to 16.9 and 12.1 µM at 6 and 50 cm, respectively with higher Fe(II) concentrations than Fe(III) concentrations. These concentrations decreased to 1.2 µM for Fe(II) and 11.1 µM for Fe(III), respectively at 93 cm, and then increased to 4 and 23.6 µM at 130 cm. This was followed by a decrease to 0 for both species at 163 cm. Both concentrations increased to 3.9-5.2 µM for Fe(II) and 31.5-32.9 µM for Fe(III) between 216 and 259 cm. Below this depth, Fe (II) was only measured at 476 cm (3.6 µM). Fe(III) decreased to 9.5 µM at 280 cm and increased to 24.1 µM at 325 cm. A similar pattern was observed between 368 and 476 cm, with an increase from 17.4 to 27.6 µM, and between 568 and 608 cm with an increase from 7.6 to 42.7 µM (Figure 3).

Dissolved Manganese (Mn) increased from 0.8 to 5.3 µM between 2 and 6 cm, then stabilized around 5 µM between 6 and 16 cm in BXN-B and BXN-SC (Figure 2). A minor increase to 7.2 µM occurred at 18 cm, followed by a major decrease to 0.3 µM at 24 cm. The concentration reached 8.9 µM at 26 cm, and subsequently decreased to 5.5 µM at 35 cm. Another increase to 8.4 µM occurred at 50 cm, followed by a decrease to 1.2 µM at 65 cm. In

https://doi.org/10.5194/bg-2023-62
Preprint. Discussion started: 13 April 2023

BXN-LC, the concentration peaked to 25.5 µM at 6 cm, followed by a decrease to zero at 93 cm (Figure 3). No Mn was measured below, except for a short increase to 1.9 µM at 603 cm.

In BXN-B and BXN-SC, dissolved magnesium [Mg^{2+}] concentration remained fairly constant from two to six cm depth with values around 300 µM before decreasing to 105 µM at eight cm (Figure S2). Then, the concentration increased to approximately 390 µM between 10 and 12 cm before decreasing to 233 µM at 20 cm. After a slight increase to 281 µM at 22 cm, the [Mg^{2+}] decreased to 93.6 µM at 40 cm. Finally, the concentration increased to 272 µM at 65 cm depth. In BXN-LC, the magnesium concentration increased from 399 µM at 6 cm to 1287 µM at 476 cm depth (Figure S3). This followed by a small decrease at 1100 µM at 520 cm depth and a little increase to 1306 µM at 564 cm depth. Finally, the [Mg^{2+}] concentration was equal to 1134 µM at 608 cm depth.

Calcium [Ca^{2+}] concentrations in the BXN-B and BXN-SC both showed a minor increase from 798 to 892 µM between two and four cm, before decreasing to 523 µM at eight cm depth (Figure S2). Then, concentration increased to 878 µM at 10 cm depth just before decreased to 409 µM at 20 cm depth, before a slight increase to 626 µM at 22 cm depth. This was followed by a small decrease to 470 µM at 24 cm depth, followed by an increase to 555 µM at 35 cm. A sharp decrease to 221 µM at 40 cm depth was followed by a relatively constant concentration of approximately 450 µM between 50 and 65 cm depth. In BXN-LC, [Ca^{2+}] showed a similar pattern with depth: approximately 900 µM between 6 and 50 cm (Figure S3). This followed by a small decrease at 588 µM at 93 cm and an increase to 1066 µM at 163 cm depth. The concentration stabilized around 490 µM between 216 and 280 cm before decreasing to 275 µM at 608 cm depth.

In BXN-B and BXN-SC, sodium [Na^{+}] and chloride [Cl^{-}] concentrations were constant from 2 to 6 cm depth at 473 and 486 µM respectively, before decreasing to 181 and 278 µM at 8 cm (Figure S2). Then, both concentrations increased to 3971 µM for [Na^{+}] and 2877 µM for [Cl^{-}] at a depth of 26 cm before slightly decreasing to 3852 and 2450 µM at 30 cm. This was followed by a small increase to 4227 µM for [Na^{+}] and 3101 µM for [Cl^{-}] at 35 cm depth, followed by a drop to 2737 and 2043 µM, respectively, at 40 cm depth. Between 40 and 65 cm, the concentration increased to 5061 µM for [Na^{+}] and 3906 µM for [Cl^{-}].

In BXN-LC, the concentration was of 1724 µM for [Na^{+}] and 1510 µM for [Cl^{-}] at 6 cm (Figure S3). A maximum concentration of 3747 µM for Na^{+} and 5386 µM for Cl^{-} was observed at 50 cm. This was followed by a decrease to 2018 and 2896 µM respectively at 93 cm. Both concentrations progressively decreased, reaching their minima of 1180 µM at 259 cm for [Na^{+}] and of 1649 µM for [Cl^{-}] at 368 cm. [Na^{+}] increased from 259 cm down to the bottom of the core, reaching a value of 4326 µM at 608 cm depth. The chloride concentration [Cl^{-}] increased between 368 and 608 cm depth, reaching a maximum of 3203 µM at the bottom of the core.

https://doi.org/10.5194/bg-2023-62
Preprint. Discussion started: 13 April 2023

303

304 Microbial and enzymatic activities

305 Measurement of microbial activity in surface biofilms showed active cells. For diatoms, microscopy of TTC
306 stained samples revealed metabolically active organelles (e.g., mitochondria) and FDA staining revealed areas
307 near the nucleus (e.g. lipid droplets; Figure S1). TTC reduction rates were high in BXN-B and BXN-SC at
308 approximately 6 cm depth, displaying rates of $1.4.10^{-4}$ mol.h^{-1}.g wet sed^{-1} and $1.5.10^{-4}$ mol.h^{-1}.g wet sed^{-1} at depth
309 of 1 and 2 cm respectively (Figure 4). Deeper in the cores, the activity decreased to $2.6.10^{-5}$ mol.h^{-1}.g wet sed^{-1} at
310 3 cm depth, and then increased to $1.9.10^{-4}$ mol.h^{-1}.g wet sed^{-1} between depths of 4 and 25 cm. Metabolic activity
311 measured with TTC decreased to $2.8.10^{-5}$ mol.h^{-1}.g wet sed^{-1} between 28 and 40 cm, and increased slightly to
312 $7.3.10^{-5}$ mol.h^{-1}.g wet sed^{-1} at 50 cm. The metabolic activity remained constant around $2.2.10^{-5}$ mol.h^{-1}.g wet sed^{-1}
313 at 60 and 65 cm.
314 In BXN-LC, TTC reduction rate was of $1.4.10^{-4}$ mol.h^{-1}.g wet sed^{-1} at 6 cm depth. It decreased to $2.1.10^{-5}$ mol.h^{-1}.g
315 wet sed^{-1} at 50 cm (Figure 5). The metabolic activity subsequently increased to $1.5.10^{-4}$ mol.h^{-1}.g wet sed^{-1} between
316 50 and 130 cm. The rate of TTC reduction was low at 163 cm depth with a value of $2.7.10^{-5}$ mol.h^{-1}.g wet sed^{-1},
317 and slightly increased to $7.3.10^{-5}$ mol.h^{-1}.g wet sed^{-1} at 216 cm. The metabolic activity decreased to
318 $4.4.10^{-5}$ mol.h^{-1}.g wet sed^{-1} at 259 cm and again to $1.3.10^{-4}$ mol.h^{-1}.g wet sed^{-1} at 280 cm. The reduction of TTC
319 then stabilized around $6.5.10^{-5}$ mol.h^{-1}.g wet sed^{-1} between 325 and 368 cm and decreased again to $1.7.10^{-5}$
320 mol.h^{-1}.g wet sed^{-1} until 476 cm. The metabolic activity subsequently increased to $4.2.10^{-5}$ mol.h^{-1}.g wet sed^{-1}
321 between 476 and 564 cm depth, and to $1.1.10^{-5}$ m mol.h^{-1}.g wet sed^{-1} at 608 cm.
322 The hydrolytic activity as measured with the FDA assay was comprised between $2.93.10^{-5}$ mol.h^{-1}.g wet sed^{-1} and
323 $3.32.10^{-5}$ mol.h^{-1}.g wet sed^{-1} at the top of BXN-B and BXN-SC, between 1 and 5 cm depth (Figure 4). Then the
324 activity progressively decreased to $1.2.10^{-5}$ mol.h^{-1}.g wet sed^{-1} between 10 and 35 cm. The rate of FDA hydrolysis
325 increased and remained approximately constant around $1.8.10^{-5}$ mol.h^{-1}.g wet sed^{-1} between 40 and 65 cm. In
326 BXN-LC, the hydrolytic activity was relatively high at 6 cm, reaching $2.9.10^{-5}$ mol.h^{-1}.g wet sed^{-1}, and
327 subsequently decreased to $1.3.10^{-5}$ mol.h^{-1}.g wet sed^{-1} at 93 cm (Figure 5). The hydrolysis rate increased to
328 $1.8.10^{-5}$ mol.h^{-1}.g wet sed^{-1} at 130 cm, remained relatively stable approximately $1.4.10^{-5}$ mol.h^{-1}.g wet sed^{-1}
329 between 163 cm and 259 cm, before dropping to $1.1.10^{-5}$ mol.h^{-1}.g wet sed^{-1} at 280 cm. The hydrolytic activity
330 increased and remained constant around $1.9.10^{-5}$ mol.h^{-1}.g wet sed^{-1} between 325 cm and 433 cm, decreased to
331 $8.4.10^{-6}$ mol.h^{-1}.g wet sed^{-1} at 476 cm. The rate of FDA hydrolysis increased to $1.2.10^{-5}$ mol.h^{-1}.g wet sed^{-1} at 520
332 cm and stabilized at $1.7.10^{-5}$ mol.h^{-1}.g wet sed^{-1} between 564 and 608 cm depth.

https://doi.org/10.5194/bg-2023-62
Preprint. Discussion started: 13 April 2023

Isothermal calorimetric (IMC) measurements of microbial activity are presented in Table 1. The growth rate (μ) value was 0.17 h^{-1} at 6 cm, increased to 0.24 h^{-1} at 50 cm and then decreased to 0.13 h^{-1} at 93 cm. The lag time was equal to 0 at 6 and 93 cm, while reaching 3.5 h at 50 cm depth. The total heat released during the experiment (Q), was equal to 5.4 J at 6 cm depth, 4.2 J at 50 cm and 2.6 J at 93 cm. The maximum metabolic activity (maxHF) was equal to 75 μW at 6 cm, 89.5 μW at 50 cm and 62.5 μW at 93 cm depth. Finally, colony-forming unit (CFU) count after 30 days of incubation was of $5.3.10^8$ at 6 cm depth, $2.8.10^7$ at 50 cm depth and $2.9.10^8$ at 93 cm depth. According to our data it appears that several strains can not be cultured in oxic conditions.

XRF sediment measurement

In BXN-B and BXN-SC, a small peak of sulfur was observed in XRF at approximately 8 cm depth (868 cps; Figure 6). This was followed by a zone between 15 and 38 cm deep with a large sulfur amount (675-1464 cps). Sulfur decreased then until 319 cps at 40 cm depth after which the sulfur amount increased and stabilized around 600 cps. The amount of manganese varied downcore. The manganese quantity was large between 0 and 3 cm depth (2785-3716 cps), after which it decreased to 1313 cps at 10 cm depth. The manganese amount then increased to 3732 at 17 cm before stabilizing between 18 and 28 cm depth (around 3481 cps). The amount of manganese decreased to 1688 cps at 31 cm depth before increasing up to 4426 cps at 33 cm. The manganese amount in the sediment decreased then to 1271 cps at 39 cm before increasing at 5182 cps at 42 cm and stabilizing between 43-45 cm (around 4000 cps). Finally, the manganese quantity decreased and remained stable around 2830 cps downcore. The quantity of aluminum in sediments increased to 4456 cps at 2 cm depth and decreased to 2412 cps at 4 cm. The amount stabilized then between five and 14 cm before it increased to around 3634 cps between 15 and 37 cm. It decreased to 2454 cps at 38 cm and remained stable between 39 and 41 cm. The aluminum amount increased at 42 cm (4880 cps) and remained around 4289 cps between 43 and 46 cm. A small decrease was noted at 47 cm (2259 cps). The aluminum quantity remained stable between 49 and 56 cm (around 3463 cps) before decreasing towards the bottom of the core. Finally, the amount of iron in sediments was relatively high between 0 and 2 cm depth ($1.13.10^5$ cps), then decreased to around $4.89.10^4$ cps between 3 and 14 cm. The quantity of iron increased then to $1.05.10^5$ cps at 15 cm before stabilizing around $9.16.10^4$ cps between 16 and 37 cm. The quantity decreased to $3.91.10^4$ cps at 39 cm and stabilized between 39 and 41 cm. The iron amount increased to $1.27.10^5$ cps at 42 cm and remained stable until 46 cm. The amount was low between 47 and 48 cm ($3.75.10^4$ cps) before increasing to $8.94.10^4$ cps at 49 cm. It remained stable between 50 and 56 cm (around $8.13.10^4$) and decreased then until downcore.

https://doi.org/10.5194/bg-2023-62
Preprint. Discussion started: 13 April 2023

In BXN-LC, XRF results showed that the amount of sulfur in sediments peaked several times at approximately 50, 150, 280, 550 and 600 cm depth (around 1000 cps; Figure S4). A depth horizon with a lower sulfur content was observed between 325 and 425 cm (around 250 cps) depth and the sediments were enriched in sulfur between 430 and 608 cm (around 600 cps). The amount of aluminum in sediments seemed rather stable between 0 and 200 cm before gradually increasing down to the bottom of the core. The manganese content remained relatively constant as well, although three peaks were found at 100, 300 and 450 cm depth (around 7500 cps). The amount of iron varied greatly with depth, with low values between 60-80, 130-150, 250-320, 360-450 and 500-530 cm depth (around 35 000 cps) and high values between 80-140, 160-250, 320-410, 450-500 and 530-608 cm depth (around 150 000 cps).

Statistical analyses of porewater geochemistry and microbial activity

The first axis of the PCA for data in both BXN-B and BXN-SC cores explained 39.6% of the variation and the second axis accounted for 19.7% of the variation (Figure 7). The correlation analyses revealed four groups of variables: (i) chlorine, pH, depth and sulfide were opposed to (ii) sulfate, and oxygen on axis 1. On axis 2 (ii) manganese, TTC, FDA, and magnesium were opposed to (iv) nitrates. In the matrix of correlation (PCA), correlations are considered as significant when $p<0.05$. The correlation matrix of the BXN-B and BXN-SC (Figure 7; n=18 samples) showed significant correlations between core depth and most of the ions analyzed. Magnesium, calcium, nitrate, sulfate and oxygen were anti-correlated with depth (correlation coefficients of r=-0.23, r=-0.62, r=-0.34, r=-0.61 and r=-0.60 respectively). Chloride, sulfide and pH were positively correlated with depth (r=0.89, r=0.23 and r=0.41 respectively). Magnesium was correlated with calcium (r=0.64) and manganese (r=0.56). Calcium was anti-correlated with the elements that increased with depth (e.g., sulfide, r=-0.70) and correlated with the elements that decreased with depth (e.g., sulfate, r=0.44). Chloride followed the opposite trend, being positively correlated with, e.g., pH (r=0.57) and negatively correlated with, e.g., sulfate (r=-0.83). Nitrate was positively correlated with sulfate (r=0.51) and oxygen (r=0.53). Sulfate was positively correlated with oxygen (r=0.72) and negatively correlated with sulfide (r=0.69), pH (-0.52) and iron (r=-0.48). Oxygen was anti-correlated with sulfide (r=-0.74), pH (r=-0.64) and iron (r=-0.30). Sulfide was positively correlated with pH (r=0.73) and iron (r=0.07) and negatively correlated with FDA (r=-0.46). pH was correlated with iron (r=0.27) and anti-correlated with FDA (r=-0.70). Manganese was correlated with FDA (r=0.37). Finally, TTC was correlated with TTC (r=0.55).

The first two axes of the PCA for BXN-LC explained respectively 36.8% and 20.6% of the variation (Figure 8). Physicochemical properties of EPS data taken from the similar core and published previously (Duteil et al. 2022)

https://doi.org/10.5194/bg-2023-62
Preprint. Discussion started: 13 April 2023

were used as a proxy for organic carbon produced in biofilms. For detail about measurements, refer to Duteil et al., 2022. In this Gironde diatom-rich surface biofilm, concentrations of colloidal EPS were 16.5 µg std eq. g dry sediment^{-1} for neutral sugars and 37.6 µg std eq. g dry sediment^{-1} for proteins. EPS concentration decreased to a depth of 50 cm after which they remained low (< 2.8 µg std eq. g dry sediment^{-1} for neutral sugars and < 3.5 µg std eq. g dry sediment^{-1} for proteins) with only a few samples having relatively high EPS concentrations, e.g. 35.7 µg std eq. g dry sediment^{-1} for protein and 6.6 µg std eq. g dry sediment^{-1} for neutral sugars at 430 cm depth. The correlation analyses revealed three groups: (i) physico-chemical EPS properties in the positive part of both axes, (ii) a large group including manganese, nitrate, iron Fe(II), calcium and chloride in the negative part of axis 1 and (iii) depth and magnesium. The correlation matrix of BXN-LC porewater data (n=16 samples) is shown Figure 8. Sulfate, nitrate, chloride, calcium, manganese and Fe(II) were anti-correlated with depth (correlation coefficient of r=-0.53, r=-0.70, r=-0.14, r=-0.83, r=-0.56 and r=-0.52 respectively) contrary to magnesium (r=0.93) and FeIII (r=0.22). EPS proteins were correlated with acidic sites (r=0.78), neutral sugars (r=0.76) and anti-correlated to TTC (r=-0.29) and sulfate (r=-0.30). EPS neutral sugars were positively correlated with and acidic sites (r=0.75) and negatively correlated with TTC (r=-0.31). EPS acidic site density was anti-correlated with TTC (r=-0.30) and sulfate (r=-0.26). TTC was positively correlated with sulfide (r=0.26) and FDA negatively correlated to Fe II (r=-0.29). Fe II was correlated with the elements that decreased with depth (e.g. nitrate, r=0.77). Fe III was positively correlated with magnesium (r=0.31) and anti-correlated with magnesium (r=-0.24), calcium (r=-0.37) and sulfide (r=-0.32). Manganese was positively correlated with calcium (r=0.59), chloride (r=0.39) and nitrate (r=0.83) but negatively correlated with magnesium (r=-0.62). Magnesium was anti-correlated with nitrate (r=-0.70), sulfate (r=-0.53) and calcium (r=-0.86). Calcium was positively correlated with the elements that decreased with depth (e.g. nitrate, r=0.67). Chloride was correlated with nitrate (r=0.56) and finally, nitrate was correlated with sulfide (r=0.27).

Precipitation-dissolution modeling

Saturation indices were calculated independently using Phreeqc for (i) BXN-B plus BXN-SC, which include sulfide measurements (Table 2) and (ii) BXN-LC (Table 3). In BXN-B and BXN-SC, the porewater was undersaturated for ferrihydrite $(Fe(III)_{10}O_{14}(OH)_2$ or $Fe(OH)_3$; saturation index (SI) -5.19 to -7.35; -6 on average; Table 2) and for goethite (α-Fe(III)O(OH); SI -1.34 to 0.41; -0.4 on average). The porewater in both cores was supersaturated for hematite at depth greater than 22 cm (Fe_2O_3; SI 0.67 to 2.78) and alternated between under- and supersaturated at greater depths/deeper in the cores. Porewater was close to equilibrium with calcite ($CaCO_3$; SI -

https://doi.org/10.5194/bg-2023-62
Preprint. Discussion started: 13 April 2023

0.49 to 0.28; 0.07 on average). The saturation was variable for sulfide minerals: mackinawite ($Fe_{1+x}S$) was undersaturated above six cm depth (-2.82 to -3.44) and supersaturated below 6 cm (SI 0.18 to 2.15); pyrite (FeS_2) was supersaturated at all depth, with significantly lower values above 6 cm (SI 1.76 to 2.53) than below (SI 8.47 to 10.57).

Sulfide measurements were lacking from BXN-LC, and thus we calculated saturation indices for iron oxides and carbonates only (Table 3). Porewaters were largely supersaturated for goethite (SI 7.25 to 9.33; 8.6 on average) and hematite (SI 16.47 to 20.62; 19.11 on average), and much less for ferrihydrite (1.65 to 3.73; 3 on average). Porewaters were close to equilibrium for calcite (SI 0.02-0.55; -0.18 on average) and for siderite ($FeCO_3$) (-1.05 to 0.91; -0.38 on average). Saturation indices were also slightly positive for dolomite (saturation index between 0.15 and 1.08 with 0.74 on average).

Discussion

Geochemical gradients as a response to the layering of microbial communities and early diagenesis

The following section describes the potential geomicrobiological reactions as a function of depth and their roles in early diagenetic processes. This discussion of our observations is organized according to the typical sequence of reduction of electron acceptors with depth (e.g., Megonigal et al., 2003).

Oxygen

The peak of [O_2] between zero and one millimeter was found in the diatom biofilm formed at the surface of the sediment (Figure 2), and indicated active oxygenic photosynthesis (Revsbech et al., 1986; Visscher & Van Gemerden 1991). Estuarine diatoms secrete a large amount of organic matter, mainly in the form of low molecular weight organic carbon (LMWOC) and exopolymeric substances (EPS; Underwood & Kromkamp, 1999; Thornton et al., 2002). LMWOC and EPS are a major product of inorganic carbon fixation in intertidal biofilms (Decho, 1990) and constitute an important source of carbon and energy for microorganisms performing aerobic and anaerobic respiration (McKew et al., 2013; Visscher et al. 1998, Braissant et al. 2009). Therefore, the amount of EPS in the sediment (from Duteil et al., 2022) is used here as a proxy for organic carbon sources. In order to simplify the following biogeochemical reactions, EPS and other sources of organic matter (e.g., LMWOC) are here considered as CH_2O.

https://doi.org/10.5194/bg-2023-62
Preprint. Discussion started: 13 April 2023

454 EPS is a major source of carbon for heterotrophic bacteria at depth (Braissant et al., 2009), that are able to degrade
455 fastly (e.g., within hours) EPS extracted from estuarine diatom biofilm under both oxic and anoxic conditions
456 (Bohórquez et al., 2017). Under oxic conditions, EPS and other carbon sources, are consumed by heterotrophic
457 bacteria through aerobic respiration, following the simplified reaction (Stumm & Morgan, 1996; Hulth et al., 1999;
458 Dupraz & Visscher 2005; Visscher & Stolz 2005):
459 $CH_2O + O_2 = CO_2 + H_2O$; $\Delta G^{o'} = -479$ kJ.mol^{-1}.
460 The depletion of oxygen indicated that this metabolism was mainly active above four centimeters in the studied
461 estuarine point bar (Figure 2C). FDA hydrolysis rate was high between 0-1 centimeter (Figure 4), indicating
462 potential enzymatic degradation of organic carbon (Battin, 1997). High TTC reduction rates confirmed that the
463 upper two centimeters were associated with a very active microbial community (Figure 4; Braissant et al., 2020),
464 similar in magnitude to hypersaline microbial mats (Braissant et al., 2009). Audry et al. (2006) also linked the
465 depletion of O_2 to aerobic respiration in the liquid mud accumulating in the Garonne estuarine channel. In the
466 channel however, aerobic respiration is considered as highly transient because the mobile mud layer is renewed
467 every tidal cycle. Sediments are much more stable on the estuarine point bars, with sedimentation rates of 2-4 cm^{-1}
468 measured in the studied area (Virolle et al., 2021).
469
470 Nitrate:
471 Nitrate is generally consumed by heterotrophic bacteria through denitrification. Denitrification has been reported
472 in estuarine sediments between 0-10 cm depth in the Colne estuary (UK, Dong et al., 2000) and Patuxent estuary
473 (USA, Jenkins & Kemp, 1984). Denitrification is typically found at low oxygen or in anaerobic conditions, and
474 could be formulated as (Stumm & Morgan, 1996; Hulth et al., 1999; Megonigal et al., 2004; Visscher & Stolz,
475 2005):
476 $5\ CH_2O + 4\ NO_3^- + 4\ H^+ = 5\ CO_2 + 2\ N_2 + 7\ H_2O$
477 or
478 $5\ CH_2O + 4\ NO_3^- = CO_2 + 2\ N_2 + 4\ HCO_3^- + 3\ H_2O$; $\Delta G^{o'} = -448$ kJ.mol^{-1}
479 Morelle et al., (2022) demonstrated that microbes from intertidal mudflat sediments (Seine estuary mouth, France)
480 used labile EPS as electron donor for nitrate reduction. This could explain the decrease in the amount of EPS
481 observed between zero and 50 cm depth (Figure 5). Fernandes et al. (2016) found that denitrification was the main
482 loss of nitrogen in intertidal sediments in the Arcachon Bay (France). Using isotopically-labeled N compounds in
483 slurry experiments, these authors measured denitrification rates ranging from 87.3 to 847 µmol.L^{-1}.d^{-1}.

https://doi.org/10.5194/bg-2023-62
Preprint. Discussion started: 13 April 2023

Consequently, denitrification could explain the absence of nitrate in the top six centimeters in the Bordeaux North point bar in our study (Figure 2) and explain the observed microbial activity (Table 1). In addition to nitrate respiration, assimilatory nitrate reduction can also take place and provides ammonia as end product, which can be used for biomass production (Megonigal et al., 2003). In the current study, denitrification under anoxic conditions probably occurred between 8 and 16 cm below the sediment surface, as suggested by the decrease in nitrate concentration at that depth interval (Figure 2) and active microbial community displayed by TTC reduction (Figures 4).

Porewater showed a peak in nitrate concentration at eight centimeters, which is in the anoxic part of the core (Figure 2). In natural conditions, nitrification generally occurs at the interface between the oxic and anoxic zones, the nitrification process being controlled by the availability of ammonium and oxygen (Dong et al., 2000). Coupled nitrification and denitrification metabolisms are common and have been documented in, e.g., the Patuxent (USA; Jenkins & Kemp, 1984), the Colne (UK; Dong et al., 2000), and the Noosa (Australia; Chen et al., 2020) estuaries. Similarly, coupled nitrification/denitrification reactions were reported in an intertidal sediment of the Arcachon Bay (France), but were limited to the surface two centimeters of the sediment in which oxygen may still diffuse (Fernandes et al., 2016). The peak occurred below a sandy permeable horizon (between 2.3 and 6 cm, Figure 2) that could be subject to advective oxygen-containing porewater locally reoxidizing the sediment (Beck et al., 2008). If oxygen was available for, e.g., aerobic ammonium oxidation that resulted in nitrate production, the following metabolic reaction could be supported (Jetten et al., 1998):

$2O_2 + NH_4^+ = NO_3^- + H_2O + 2H^+$; $\Delta G^{o\prime} = -349$ kJ.mol^{-1}

The sulfate concentration decreased between two and six cm depth (Figure 2), indicating sulfate reduction took place. The sulfides formed as a product are known inhibitors of denitrification (Sorensen et al., 1980) and could have diffused through the permeable sandy horizon, inhibiting denitrification (Joye & Hollibaugh, 1995). This would result in accumulation of nitrate. Alternatively, the nitrate peak observed in the current study occurred in the anoxic part of the sediment core and coincided with a high manganese concentration and increased pH values (Figure 2). These conditions could support anoxic nitrification coupled to manganese reduction, which had been reported in marine and estuarine sediments (Hulth et al., 1999; Bartlett et al., 2008). The reaction equation is as follows (Hulth et al., 1999):

$4MnO_2 + NH_4^+ + 6H^+ = NO_3^- + 2Mn_2^+ + 5H_2O$; $\Delta G^{o\prime} = -175$ kJ.mol^{-1}

Sulfate:

https://doi.org/10.5194/bg-2023-62
Preprint. Discussion started: 13 April 2023

In BXN-B and BXN-SC, the concentration of sulfate decreased sharply below 10 cm and was close to zero at 22 cm, 26 cm and 50 cm depth (Figure 2). The first sulfate minimum coincided with a peak in sulfide at approximately 20 cm depth. Similar decreasing trends in porewater sulfate concentration with depth were common in the Chesapeake Bay sediments (USA; Burdige & Zheng, 2003) and in the Harvey and Peel–Harvey estuaries (Australia; Kraal et al., 2013). Sulfate reduction in sediments can be simplified as follows (Stumm & Morgan, 1996; Hulth et al., 1999; Megonigal et al., 2003; Baumgartner et al., 2006):

$2CH_2O + SO_4^{2-} + H^+ = 2CO_2 + HS^- + 2H_2O$ ($\Delta G^{o'} = -457.7$ kJ.mol^{-1})

Sulfate reduction is one of the major pathways for organic matter mineralization in coastal and estuarine environments (Thode-Andersen & Jorgensen, 1989; Luther et al., 1992; Megonigal et al. 2003). Thus, Jiang et al. (2009) found in the Pearl estuary (China), that sulfate reducing bacteria (SRB) were present in the sediment at all depths between 0 and 50 cm, but their 16S rRNA genes were particularly abundant at intermediate depth (6-40 centimeters). In the Gironde estuary, sulfate showed a reverse trend to the sulfide concentration and pH between six and 22 cm, which could be explained by active sulfate reduction at this depth (Figure 2). This depth horizon was also characterized by a progressive increase in metabolic activity determined by TTC reduction, reaching a maximum at 20-25 cm (Figure 4) as well as evidence of microbial activity at 50 cm depth (Table 1). Similar observations based on microbial activity measurements and abundance of SRB at the oxic to anoxic transition zone in the Gloucester Beach subterranean estuary (Chesapeake Bay, USA) were reported by Hong et al (2019). SRB cultures isolated from intertidal sediments of the River Forth estuary (Scotland) could degrade xanthan, which is often used as analog for EPS (Battersby et al., 1984). The decrease in EPS concentrations observed between zero and 50 cm in BXN-LC (Duteil et al., 2022) could be explained by (partial) consumption of EPS by sulfate reducers (Braissant et al., 2009).

Two small sulfate peaks at 163 cm (10 µM) and 280-325 cm (around 4 µM) could be observed in BXN-LC associated with a layer of mixed sandy and muddy deposits (Figure 3). Small peaks of nitrate and sulfate were also associated with similar permeable sand/mud facies at 130 and 325 cm depth (Figure 3). Based on conservative tracers, sodium and chloride that can be used as proxies for contamination or mixing of porewater (Martin, 1999), our data suggested moderate salinity variations and no major freshwater intrusion (Figures 2 and 3; Martin et al., 2004). Nevertheless, the relatively permeable horizons could be subject to porewater intrusion from, e.g., the channel bank, locally reoxidizing the sediment (Beck et al., 2008). The peaks of nitrate and sulfate were found at the same depth as or just below peaks of TTC reduction (130 and 280 cm; Figure 5), indicating possible sulfate

https://doi.org/10.5194/bg-2023-62
Preprint. Discussion started: 13 April 2023

and nitrate reduction activity. The sulfide produced by SRB could react with iron or manganese oxides according to the following equations (Canfield et al., 1993):

$H_2S + 4H^+ + 2FeOOH = S^0 + 2Fe^{2+} + 4H_2O$

and

$H_2S + 2H^+ + MnO_2 = Mn^{2+} + S^0 + 2H_20$.

Sulfide could also interact with dissolved Fe(II) to produce amorphous and metastable iron sulfide phases such as mackinawite:

$Fe^{2+} + HS^- = FeS + H^+$ (Jorgensen & Nelson, 2004).

Or stable phases such as pyrite:

$FeS + H_2S = FeS_2 + H_2$ (Kraal et al. 2013)

Both mackinawite and pyrite were found in eutrophic and organic-rich salt marsh and estuarine sediments (Sorensen & Jorgensen, 1987; Luther et al., 1992; Kraal et al., 2013) similar to the Gironde estuary. In this study, we did not used techniques allowing for identification of poorly crystalline iron sulfides (e.g., mackinawite, greigite), but the presence of solid iron and sulfur documented with XRF between 15 and 37 cm depth (Figure 6) could indicate the potential precipitation of such minerals. Framboidal pyrite crystals have been locally identified in clay grain coats of Bordeaux North point bar by Virolle et al., (2021). PhreeQc modeling indicated that porewater was undersaturated with respect to mackinawite between the surface and 10 cm depth, but supersaturated deeper into the sediment column (Table 2). A shift in SI for pyrite was also observed at 10 cm, which was slightly supersaturated above 10 cm depth and supersaturated down to at least 65 cm depth. However, no major pyrite precipitation was observed in this zone despite this supersaturation. In the Gironde estuary, pyrite accounted for 0.3 to 1% of the sediment volume in the estuary funnel tidal sand bar (Virolle et al., 2020), and for 0.6% of the sediment volume in the Bordeaux Nord point bar (Virolle et al., 2021). In similar settings pyrite represented less than 0.7% of the sediment in the Ravenglass Estuary (UK; Griffiths et al., 2018). In tidal sands from the Gironde, pyrite was mostly found in the framboidal form within detrital clay coats (Virolle et al., 2020), indicating a potential relationship with EPS degradation. The precipitation rate of pyrite in natural sediments is usually much slower than the rate predicted by kinetic equations. Instead, the dominant phases that precipitate are generally metastable iron sulfides (Kraal et al., 2013).

Although we did not measure CH_4, methanogenesis is also a common process in estuaries (O'Sullivan et al., 2013; Hong et al., 2019). It is plausible that methanogenesis occurs outside sulfate reduction zones, i.e., essentially between 50 and 93 centimeters, 2.16 and 2.59 meters, and below 3.68 meters depth. Hong et al. (2019) showed an

https://doi.org/10.5194/bg-2023-62
Preprint. Discussion started: 13 April 2023

increase in methanogenic archaeal gene abundance below 70 centimeters in an estuary in Gloucester Beach (USA), supporting the notion that methanogenesis could occur in zones of low or no sulfate in the Bordeaux North point bar sediments.

Manganese

River water input is a major source of Fe and Mn oxides. The most labile fraction of these oxides can be recycled and dissolved, typically within months in surface sediments of estuaries (Audry et al., 2007; De Chanvalon et al., 2016). Redox boundaries downcore are characterized by the (re) precipitation of manganese and iron mineral phases (Burdige, 1993). In both BXN-B and BXN-SC, the concentration of Fe(II) was greater between six and 50 cm than the Fe(III) concentration at that depth interval (Figure 2), which indicated reducing (e.g., negative E^o) conditions. The depletion of dissolved iron and manganese between 20 and 25 cm in BXN-B and BXN-SC could be related to an active redox interface associated with the precipitation of metals (Figure 2). A second zone of dissolved Mn and Fe depletion at 35 cm depth could reflect another zone of precipitation (Burdige, 1993). Similar multiple precipitation zones were observed in the consolidated sediments of the Gironde estuarine channel (Audry et al., 2006), as well as in other estuaries (Widerlund & Ingri, 1996; Oldham et al., 2019). The peaks in manganese concentration between 2-6 cm, 16-18 cm and 35-50 cm depth (Figure 2) could also be explained by organic carbon degradation supported by manganese oxide reduction. This could occur under anaerobic conditions (Burdige, 1993) according to the following reaction (Stumm & Morgan, 1996; Hulth et al., 1999):

$$CH_2O + 3CO_2 + H_2O + 2MnO_2 = 2Mn^{2+} + 4HCO_3^-;\ \Delta G^{o'} = -190\ kJ.mol^{-1}$$

Manganese-reducing microorganisms have been found in coastal marine (Burdige & Nealson, 1985) and estuarine sediments polluted with mining effluent (Pereira, 2017). Under anoxic conditions, some microbes are capable of coupling manganese oxide reduction to other oxidants than metals, for example sulfide (Aller & Rude, 1988), a process that also occurs abiotically (Thamdrup et al., 1994). The latter mechanism could explain the manganese and sulfide profiles in the Gironde estuary (Figure 2). No dissolved manganese was found below one-meter depth (Figure 3), indicating that Mn cycling was only active above this depth.

Manganese oxides (or oxyhydroxides) are typically referred to as MnOx (x>1). The predominant Mn oxides found in estuarine sediments were todorokite and vernadite (Burdige, 1993). Mn oxides are amorphous and often found as coatings on sedimentary particles (e.g., sand grains; Burdige, 1993). Manganese oxidation can be produced through abiotic reactions, e.g., with dissolved O_2, or photochemically, but could also result from reactions with super-oxidants produced extracellularly by bacteria (e.g., superoxide; Learman et al., 2011). Dissolved Mn tends

https://doi.org/10.5194/bg-2023-62
Preprint. Discussion started: 13 April 2023

603 to diffuse upward and reoxidize, and precipitate with other oxides or carbonates, or can be released to the water
604 column in estuaries (Burdige, 1993; Audry et al., 2006; De Chanvalon et al., 2016). Abiotic reduction of
605 manganese oxides could also explain the variation of the Mn observed in the uppermost meter of the core (Figures
606 2 and 3). The manganese, sulfide and iron cycles are typically tightly coupled and Fe(II) can be abiotically oxidized
607 by manganese oxides through the reaction:
608 $MnO_2 + 2Fe^{2+} + 2H_2O = Mn^{2+} + 2FeOOH + 2\ H^+$ (Kappler et al, 2021).
609 However, the correlation between dissolved iron and manganese in BXN-B and BXN-SC (p-value>0.05, r=0.29;
610 Figure 7) and in BXN-LC (p-value>0.05, r=0.68; Figure 8) indicated that this reaction is probably not prevalent
611 in the sediments studied here. Below 50-60 cm depth, dissolved Mn concentrations remained close to zero,
612 indicating a potential stability of Mn-bearing mineral phases. This was confirmed by the distinctive Mn mineral
613 peaks measured by XRF in BXN-LC at ca. 100, 290 or 460 cm (Figure S4).
614
615 Iron:
616 Microbially-mediated Fe(III) reduction is a common metabolism in estuarine and coastal sediments (Tugel et al.,
617 1986; Canfield et al., 1993; Kappler et al., 2021), and is depicted as follows (Stumm & Morgan, 1996; Hulth et
618 al., 1999):
619 $CH_2O + 4Fe(OOH) + H_2O = HCO_3^- + 4Fe^{2+} + 7OH^-$; $\Delta G^{o'} = -97\ kJ.mol^{-1}$
620 Iron reduction can also be achieved chemically using electron donors such as sulfide (Burdige & Nealson, 1986).
621 The Fe(III) peaks could indicate active iron reduction at 10-18 cm, 24-26 cm and 35-50 cm depth in BXN-B and
622 BXN-SC (Figure 2). Some of these peaks coincided with the high metabolic activities between 10 and 28 cm as
623 measured with TTC (Figure 4). Similar observations were made in BXN-LC, where increases in concentration of
624 Fe(III) could be related to high metabolic activity (e.g., at 130 cm and 280 cm depth; Figure 5).
625 In contrast to the depth profiles of Mn, dissolved Fe(III) concentrations showed an increase with depth. The
626 oxidation of Fe^{2+} and the presence of Fe^{3+} ions lead to the precipitation of iron hydroxides, oxyhydroxides or
627 oxides (FeOOH) depending on specific environmental conditions of, e.g, pH and Eh (Stumm & Morgan, 1996;
628 Cudennec & Lecerf, 2006). Iron oxides associated with estuarine or marine sediments are generally metastable
629 and poorly crystalline (Burdige, 1993). Among these oxides, ferrihydrite ($Fe(OH)_3$) is a metastable phase that can
630 transform to goethite (FeO(OH)) or hematite (Fe_2O_3). Hematite formation is favored at neutral conditions
631 (Cudennec & Lecerf, 2006). The maximum rate of hematite precipitation occurs between pH seven and eight
632 (Schwertmann & Murad, 1983), which is a typical range in estuarine environments (El Ghobary, 1983; Stumm &

https://doi.org/10.5194/bg-2023-62
Preprint. Discussion started: 13 April 2023

633 Morgan, 1996; Kraal et al., 2013; Fiket et al., 2019; Figure 2). Modeling demonstrated BXN-B and BXN-SC
634 porewater was largely undersaturated with respect to ferrihydrite, slightly undersaturated or close to equilibrium
635 with goethite, and locally supersaturated for hematite, especially between depths from zero to 18 cm (Table 2). In
636 BXN-LC, porewater was supersaturated with respect to iron oxides, slightly supersaturated for ferrihydrite, and
637 largely supersaturated for hematite (SI up to 20.62; Table 3). This indicated preferential hematite precipitation at
638 circumneutral pH. However, even if iron oxides precipitate in the Bordeaux point bar sediments, their actual form
639 remains poorly known. Well-crystallized iron oxides were not found using XRD but, using transmission electron
640 microscopy, Virolle (2019) observed Fe-rich nanoparticles associated with detrital clay coats. Based on low
641 proportions of ascorbate-extractable Fe (<5%), Audry et al. (2006) postulated that most Fe oxides could be in the
642 form of goethite or hematite in the Gironde estuarine channel muds.
643
644 **A conceptual geomicrobiological model**
645
646 We propose a scenario describing the interactions between microbial metabolisms, organic carbon sources
647 (including EPS) and the early diagenetic fate of metals in the sediments of the Gironde Estuary (Figure 9). In this
648 model, diatoms perform oxygenic photosynthesis in a surface biofilm (*reaction 1*; Figure 9) during which they
649 excrete large amounts of EPS. These EPS can form complexes with clay and sand particles, and are thus integrated
650 within the sediment (Duteil et al., 2020; Duteil et al., 2022). EPS constitute one of the main sources of organic
651 carbon for heterotrophs deeper in the sediment column (e.g., Braissant et al., 2007, 2009; Decho & Guttierez,
652 2017). Oxygen is consumed through aerobic respiration (*reaction 2*; Figure 9), which is the dominant heterotrophic
653 metabolism in the uppermost centimeters of the sediment. Aerobic respiration is efficient in oxidizing organic
654 matter, which is corroborated by a decrease of the EPS abundance with depth, e.g., between the sediment surface
655 and six cm depth (Figure 5). Aerobic respiration coincides with high metabolic activity as shown by TTC
656 measurements as well as high hydrolytic activity as shown by FDA measurements (Figure 4). In this zone, the low
657 concentrations of dissolved Mn and Fe indicate that these metals could be present as Fe(III) and Mn(IV)
658 (oxy)hydroxides. Once most of the oxygen is consumed (microbially and chemically), nitrate is a potential major
659 electron donor if available (i.e., if not used for biomass production). If so, denitrification (*reaction 5*; Figure 9)
660 becomes a major pathway for organic matter oxidation. Concurring peaks of nitrate and dissolved manganese at
661 10 cm depth could indicate nitrification (*reaction 3*; Figure 9), where nitrate production would be coupled to
662 manganese oxide dissolution (Hulth et al., 1999; Bartlett et al., 2008) or aerobic ammonium oxidation if local
663 reoxygenation of sediments occurs (Jetten et al., 1998). Sulfate reduction (*reaction 4*; Figure 9) is likely the

https://doi.org/10.5194/bg-2023-62
Preprint. Discussion started: 13 April 2023

664 predominant metabolism below 10 cm depth, supported by organic carbon (including EPS and LMWOC). Sulfate
665 reduction coincides with the maximum of metabolic activity as shown by TTC measurements. Sulfate reduction
666 yields dissolved sulfides, which can precipitate with metals. Sulfate reduction is highly active to a depth of at least
667 60 cm. Some metals (e.g., Mn, Fe, Al; Figure S3) and sulfide in the porewater increased in concentration, indicating
668 the potential for metal sulfide precipitation. The sulfate concentration decreased in several centimeter-thick
669 horizons (e.g., around 25 cm and 35 cm depth), which coincided with a decrease in dissolved Fe and Mn indicating
670 the potential for precipitation of these metals as sulfides. Furthermore, the consumption of organic carbon by
671 (an)aerobic heterotrophs could liberate metals from metal-organic ligand complexes, leading to their precipitation
672 (e.g., Dupraz et al., 2004; Braissant et al., 2007). The release of Fe(III) by this process would support respiration
673 by iron-reducing bacteria. Combined with local reducing conditions would result in the precipitation of Fe(II) as
674 iron sulfides (e.g., mackinawite, *reaction B*, rarely pyrite; Figure 9) and the reduction of manganese oxides
675 (*reaction C*; Figure 9). Nitrate and sulfate reduction could continue at slower rates deeper in the sediment (e.g., at
676 150 and 300 cm depth), coupled to local enrichment of metals (e.g., at 50 and 476 cm depth), possibly enhanced
677 by microbial metabolisms such as Mn and Fe reduction (*reactions 6 and 7*; Figure 9). The increase in sulfate
678 concentration at depth in the absence of oxygen may be due to dissolution of the metastable iron sulfide phase
679 (*reaction D*; Figure 9), followed by sulfide oxidation coupled to nitrate reduction (Megonigal et al. 2003). Iron
680 oxides seem limited in concentration despite porewater supersaturation around six meters depth, possibly forming
681 complexes with organic molecules and occurring as poorly crystalline and metastable colloidal phases (Norman
682 et al., 2015; Kappler et al., 2021). In sum, the biogeochemical cycles of C, S, N, Fe or Mn in the Bordeaux North
683 point bar are likely driven by a complex combination of metabolic and geochemical reactions.
684

685 ## Conclusion
686

687 Porewater and sediment chemistry, microbial and enzyme activities as a function of depth in three cores sampled
688 in a point bar of the Gironde estuary showed that the concentration of major ions (Mn^{2+}, Mg^{2+}, Ca^{2+}, Fe^{2+}, Fe^{3+},
689 HS^-, SO_4^{2-}, NO_3^-, Cl^-, Na^+) fluctuated significantly. Such fluctuations with depth could be linked to
690 biogeochemical reactions. The sequence of microbial metabolisms mostly followed the classical suite of reactions
691 following the decreasing Gibbs free energy yield provided by successively electron acceptors (i.e., oxygen, nitrate,
692 Mn and Fe oxides, sulfate). However, our results indicated that some reactions were likely coupled or at least
693 occurred concomitantly. For example, denitrification and sulfate reduction coexisted at around 10 cm depth, which

https://doi.org/10.5194/bg-2023-62
Preprint. Discussion started: 13 April 2023

could be supported by non-competitive substrates (Megonigal et al. 2003). Measurements of metabolic, enzymatic and bacterial activities confirmed or suggested the potential role of specific functional groups of microorganisms in the various reactions. While metabolic activities decreased between the surface biofilm and the zone of aerobic respiration, it increased markedly in the zone of anaerobic respiration, between 10 and 30 cm, concomitantly with significant changes in porewater (NO_3^-, HS^-, SO_4^{2-}, Mn, Fe) and sediment composition (increase in S, Fe, Mn). Based on these results, we propose the following vertical sequence of geomicrobiological reactions (i) oxygenic photosynthesis was found in the diatom biofilm at the surface of the sediment; (ii) aerobic respiration was observed down to approximately five cm; (iii) a reduction of Mn oxides was possibly coupled with nitrification (or sulfate reduction) between five and 10 cm, as indicated by the concomitant increase in dissolved Mn and nitrate. The increase in nitrate could also be due to local reoxidation or inhibition of denitrification by sulfide; (iv) nitrate was subsequently reduced between 10 and 15 cm depth; (v) sulfate reduction was active at several depth intervals, but the main sulfate reduction zone occurred between eight and 20 cm, where substantial amounts of electron donor are still available; (vi) the reduction and dissolution of iron and manganese oxides coincided with sulfate reduction, and was particularly high at 20 and 30 cm.

We documented enrichments for some metals (e.g., Fe, Mn, Ca) and sulfur in the zones of sulfate reduction, indicating potential precipitation of iron sulfides. Below one meter depth in the core, the main electron acceptors were almost completely consumed and thus microbial activity was reduced significantly. Dissolved Mn concentrations remained near zero, indicating a potential stability of the Mn-bearing mineral phases. Dissolved Fe(III) concentrations showed an increase with depth and modeling demonstrated that the pore water was supersaturated with iron oxides. Iron oxides were potentially occurring as poorly crystalline and metastable colloidal phases or could have formed complexes with organic carbon. The lack of dissolved sulfide measurements in the long core does not allow to calculate the saturation indices of sulfides, but the local observation of pyrites suggests that iron sulfides may precipitate. These results allowed us to propose a geomicrobiological conceptual model, which was more complex than the widely used classical stratification model of microbial metabolisms.

Acknowledgements

This research received funding from the programme TelluS of the Institut National des Sciences de l'Univers of the CNRS (project Elapse; coord. R. Bourillot) and from the project "ClayCoat 3", a collaborative project between Bordeaux INP and Neptune Energy.

https://doi.org/10.5194/bg-2023-62
Preprint. Discussion started: 13 April 2023

The authors thank Isabelle Billy and Olivier Ther (PAACS platform, UMR EPOC) for XRF measurements and core photographs. Maxime Virolle and Hervé Derriennic for their help during sediment coring.

References

Aller, R. C. and Rude, P. D.: Complete oxidation of solid phase sulfides by manganese and bacteria in anoxic marine sediments, Geochimica et Cosmochimica Acta, 52, 751–765, https://doi.org/10.1016/0016-7037(88)90335-3, 1988.

Audry, S., Blanc, G., and Schäfer, J.: The impact of sulphide oxidation on dissolved metal (Cd, Zn, Cu, Cr, Co, Ni, U) inputs into the Lot–Garonne fluvial system (France), Applied geochemistry, 20, 919–931, https://doi.org/10.1016/j.apgeochem.2005.01.006, 2005.

Audry, S., Blanc, G., Schäfer, J., Chaillou, G., and Robert, S.: Early diagenesis of trace metals (Cd, Cu, Co, Ni, U, Mo, and V) in the freshwater reaches of a macrotidal estuary, Geochimica et Cosmochimica Acta, 70, 2264–2282, https://doi.org/10.1016/j.gca.2006.02.001, 2006.

Bartlett, R., Mortimer, R. J. G., and Morris, K.: Anoxic nitrification: Evidence from Humber Estuary sediments (UK), Chemical Geology, 250, 29–39, https://doi.org/10.1016/j.chemgeo.2008.02.001, 2008.

Battersby, N., Stewart, D., and Sharma, A.: Effect of xanthan on the growth of sulphate-reduction bacteria in marine sediments, Colloque International de Bacteriologie Marine, Brest (France), 5, 1984.

Battin, T. J.: Assessment of fluorescein diacetate hydrolysis as a measure of total esterase activity in natural stream sediment biofilms, Science of the Total Environment, 198, 51–60, https://doi.org/10.1016/S0048-9697(97)05441-7, 1997.

Baumgartner, L. K., Reid, R. P., Dupraz, C., Decho, A. W., Buckley, D. H., Spear, J. R., Przekop, K. M., and Visscher, P. T.: Sulfate reducing bacteria in microbial mats: changing paradigms, new discoveries, Sedimentary Geology, 185, 131–145, https://doi.org/10.1016/j.sedgeo.2005.12.008, 2006.

Beck, M., Dellwig, O., Schnetger, B., and Brumsack, H.-J.: Cycling of trace metals (Mn, Fe, Mo, U, V, Cr) in deep pore waters of intertidal flat sediments, Geochimica et Cosmochimica Acta, 72, 2822–2840, https://doi.org/10.1016/j.gca.2008.04.013, 2008.

Beck, M., Reckhardt, A., Amelsberg, J., Bartholomä, A., Brumsack, H.-J., Cypionka, H., Dittmar, T., Engelen, B., Greskowiak, J., and Hillebrand, H.: The drivers of biogeochemistry in beach ecosystems: a cross-shore transect from the dunes to the low-water line, Marine Chemistry, 190, 35–50, https://doi.org/10.1016/j.marchem.2017.01.001, 2017.

Bohórquez, J., McGenity, T. J., Papaspyrou, S., García-Robledo, E., Corzo, A., and Underwood, G. J. C.: Different Types of Diatom-Derived Extracellular Polymeric Substances Drive Changes in Heterotrophic Bacterial Communities from Intertidal Sediments, Frontiers in Microbiology, 8, 245, https://doi.org/10.3389/fmicb.2017.00245, 2017.

Braissant, O., Decho, A. W., Dupraz, C., Glunk, C., Przekop, K. M., and Visscher, P. T.: Exopolymeric substances of sulfate-reducing bacteria: interactions with calcium at alkaline pH and implication for formation of carbonate minerals, Geobiology, 5, 401–411, https://doi.org/10.1111/j.1472-4669.2007.00117.x, 2007.

https://doi.org/10.5194/bg-2023-62
Preprint. Discussion started: 13 April 2023

761 Braissant, O., Decho, A. W., Przekop, K. M., Gallagher, K. L., Glunk, C., Dupraz, C., and Visscher, P. T.:
762 Characteristics and turnover of exopolymeric substances in a hypersaline microbial mat, FEMS microbiology
763 ecology, 67, 293–307, https://doi.org/10.1111/j.1574-6941.2008.00614.x, 2009.
764 Braissant, O., Bonkat, G., Wirz, D., and Bachmann, A.: Microbial growth and isothermal microcalorimetry:
765 growth models and their application to microcalorimetric data, Thermochimica Acta, 555, 64–71,
766 https://doi.org/10.1016/j.tca.2012.12.005, 2012.
767 Braissant, O., Astasov-Frauenhoffer, M., Waltimo, T., and Bonkat, G.: A review of methods to determine viability,
768 vitality, and metabolic rates in microbiology, Frontiers in Microbiology, 2726,
769 https://doi.org/10.3389/fmicb.2020.547458, 2020.
770 Burdige, D. J.: The biogeochemistry of manganese and iron reduction in marine sediments, Earth-Science
771 Reviews, 35, 249–284, https://doi.org/10.1016/0012-8252(93)90040-E, 1993.
772 Burdige, D. J. and Gieskes, J. M.: A pore water/solid phase diagenetic model for manganese in marine sediments,
773 American Journal of Science, 283, 20, https://doi.org/10.2475/ajs.283.1.29, 1983.
774 Burdige, D. J. and Nealson, K. H.: Microbial Manganese Reduction by Enrichment Cultures from Coastal Marine
775 Sediments, Applied and Environmental Microbiology, 50, 491–497, https://doi.org/10.1128/aem.50.2.491-
776 497.1985, 1985.
777 Burdige, D. J. and Zheng, S.: The biogeochemical cycling of dissolved organic nitrogen in estuarine sediments,
778 Limnology and Oceanography, 43, 1796–1813, https://doi.org/10.4319/lo.1998.43.8.1796, 2003.
779 Canfield, D. E., Thamdrup, B., and Hansen, J. W.: The anaerobic degradation of organic matter in Danish coastal
780 sediments: iron reduction, manganese reduction, and sulfate reduction, Geochimica et Cosmochimica Acta, 57,
781 3867–3883, https://doi.org/10.1016/0016-7037(93)90340-3, 1993.
782 de Chanvalon, A. T., Mouret, A., Knoery, J., Geslin, E., Peron, O., and Metzger, E.: Manganese, iron and
783 phosphorus cycling in an estuarine mudflat, Loire, France, Journal of Sea Research, 118, 92–102,
784 https://doi.org/10.1016/j.seares.2016.10.004, 2016.
785 Chatterjee, M., Silva Filho, E. V., Sarkar, S. K., Sella, S. M., Bhattacharya, A., Satpathy, K. K., Prasad, M. V. R.,
786 Chakraborty, S., and Bhattacharya, B. D.: Distribution and possible source of trace elements in the sediment cores
787 of a tropical macrotidal estuary and their ecotoxicological significance, Environment International, 33, 346–356,
788 https://doi.org/10.1016/j.envint.2006.11.013, 2007.
789 Chen, J.-J., Erler, D. V., Wells, N. S., Huang, J., Welsh, D. T., and Eyre, B. D.: Denitrification, anammox, and
790 dissimilatory nitrate reduction to ammonium across a mosaic of estuarine benthic habitats, Limnology and
791 Oceanography, 17, https://doi.org/10.1002/lno.11681, 2020.
792 Chiffoleau, J.-F., Cossa, D., Auger, D., and Truquet, I.: Trace metal distribution, partition and fluxes in the Seine
793 estuary (France) in low discharge regime, Marine Chemistry, 47, 145–158, https://doi.org/10.1016/0304-
794 4203(94)90105-8, 1994.
795 Cudennec, Y. and Lecerf, A.: The transformation of ferrihydrite into goethite or hematite, revisited, Journal of
796 solid state chemistry, 179, 716–722, https://doi.org/10.1016/j.jssc.2005.11.030, 2006.
797 De Winder, B., Staats, N., Stal, L. J., and Paterson, D. M.: Carbohydrate secretion by phototrophic communities
798 in tidal sediments, Journal of Sea Research, 42, 131–146, https://doi.org/10.1016/S1385-1101(99)00021-0, 1999.
799 Decho, A.: Microbial exopolymer secretions in ocean environments: their role (s) in food webs and marine
800 processes, Oceanogr. Mar. Biol. Annu. Rev., 28, 73–153, 1990.

https://doi.org/10.5194/bg-2023-62
Preprint. Discussion started: 13 April 2023

Decho, A. W.: Microbial biofilms in intertidal systems: an overview, Continental shelf research, 20, 1257–1273, 2000.

Decho, A. W. and Gutierrez, T.: Microbial extracellular polymeric substances (EPSs) in ocean systems, Frontiers in microbiology, 8, 922, https://doi.org/10.3389/fmicb.2017.00922, 2017.

Dong, L. F., Thornton, D. C. O., Nedwell, D. B., and Underwood, G. J. C.: Denitrification in sediments of the River Colne estuary, England, Marine Ecology Progress Series, 203, 109–122, https://doi.org/10.3354/meps203109, 2000.

Dupraz, C. and Visscher, P. T.: Microbial lithification in marine stromatolites and hypersaline mats, Trends in microbiology, 13, 429–438, https://doi.org/10.1016/j.tim.2005.07.008, 2005.

Dupraz, C., Visscher, P. T., Baumgartner, L. K., and Reid, R. P.: Microbe–mineral interactions: early carbonate precipitation in a hypersaline lake (Eleuthera Island, Bahamas), Sedimentology, 51, 745–765, https://doi.org/10.1111/j.1365-3091.2004.00649.x, 2004.

Duteil, T., Bourillot, R., Grégoire, B., Virolle, M., Brigaud, B., Nouet, J., Braissant, O., Portier, E., Féniès, H., and Patrier, P.: Experimental formation of clay-coated sand grains using diatom biofilm exopolymers, Geology, 48, 1012–1017, https://doi.org/10.1130/G47418.1, 2020.

Duteil, T., Bourillot, R., Braissant, O., Grégoire, B., Leloup, M., Portier, E., Brigaud, B., Féniès, H., Svahn, I., and Henry, A.: Preservation of exopolymeric substances in estuarine sediments, Frontiers in Microbiology, 13, https://doi.org/10.3389/fmicb.2022.921154, 2022.

El Ghobary, H.: Interstitial water chemistry of the inner continental shelf sediments off the Gironde Estuary, Estuarine, Coastal and Shelf Science, 16, 639–650, https://doi.org/10.1016/0272-7714(83)90076-8, 1983.

Fernandes, S. O., Javanaud, C., Michotey, V. D., Guasco, S., Anschutz, P., and Bonin, P.: Coupling of bacterial nitrification with denitrification and anammox supports N removal in intertidal sediments (Arcachon Bay, France), Estuarine, Coastal and Shelf Science, 179, 39–50, https://doi.org/10.1016/j.ecss.2015.10.009, 2016.

Fiket, Ž., Fiket, T., Ivanić, M., Mikac, N., and Kniewald, G.: Pore water geochemistry and diagenesis of estuary sediments—an example of the Zrmanja River estuary (Adriatic coast, Croatia), Journal of Soils and Sediments, 19, 2048–2060, https://doi.org/10.1007/s11368-018-2179-9, 2019.

Gil, M. M., Brandao, T. R., and Silva, C. L.: A modified Gompertz model to predict microbial inactivation under time-varying temperature conditions, Journal of Food Engineering, 76, 89–94, https://doi.org/10.1016/j.jfoodeng.2005.05.017, 2006.

Glud, R. N., Ramsing, N. B., and Revsbech, N. P.: Photosynthesis and Photosynthesis-coupled respiration in natural biofilms quantified with oxygen microsensors, Journal of Phycology, 28, 51–60, https://doi.org/10.1111/j.0022-3646.1992.00051.x, 1992.

Green, V. S., Stott, D. E., and Diack, M.: Assay for fluorescein diacetate hydrolytic activity: optimization for soil samples, Soil Biology and Biochemistry, 38, 693–701, https://doi.org/10.1016/j.soilbio.2005.06.020, 2006.

Griffiths, J., Worden, R. H., Wooldridge, L. J., Utley, J. E., and Duller, R. A.: Detrital clay coats, clay minerals, and pyrite: a modern shallow-core analogue for ancient and deeply buried estuarine sandstones, Journal of Sedimentary Research, 88, 1205–1237, https://doi.org/10.2110/jsr.2018.56, 2018.

Hensen, C., Zabel, M., and Schulz, H. N.: Benthic cycling of oxygen, nitrogen and phosphorus, in: Marine Geochemistry, Springer, 207–240, 2006.

https://doi.org/10.5194/bg-2023-62
Preprint. Discussion started: 13 April 2023

840 Hong, Y., Wu, J., Wilson, S., and Song, B.: Vertical stratification of sediment microbial communities along
841 geochemical gradients of a subterranean estuary located at the Gloucester Beach of Virginia, United States,
842 Frontiers in microbiology, 9, 3343, https://doi.org/10.3389/fmicb.2018.03343, 2019.
843 Hulth, S., Aller, R. C., and Gilbert, F.: Coupled anoxic nitrification/manganese reduction in marine sediments,
844 Geochimica et Cosmochimica Acta, 63, 49–66, https://doi.org/10.1016/S0016-7037(98)00285-3, 1999.
845 Jenkins, M. C. and Kemp, W. M.: The coupling of nitrification and denitrification in two estuarine sediments1,2,
846 Limnology and Oceanography, 29, 609–619, https://doi.org/10.4319/lo.1984.29.3.0609, 1984.
847 Jetten, M. S., Strous, M., Van De Pas-Schoonen, K. T., Schalk, J., Van Dongen, U. G., Van De Graaf, A. A.,
848 Logemann, S., Muyzer, G., Van Loosdrecht, M. C., and Kuenen, J. G.: The anaerobic oxidation of ammonium,
849 FEMS Microbiology reviews, 22, 421–437, https://doi.org/10.1111/j.1574-6976.1998.tb00379.x, 1998.
850 Jiang, L., Zheng, Y., Peng, X., Zhou, H., Zhang, C., Xiao, X., and Wang, F.: Vertical distribution and diversity of
851 sulfate-reducing prokaryotes in the Pearl River estuarine sediments, Southern China, FEMS microbiology ecology,
852 70, 249–262, https://doi.org/10.1111/j.1574-6941.2009.00758.x, 2009.
853 Jorgensen, B. B. and Nelson, D. C.: Sulfide oxidation in marine sediments: geochemistry meets microbiology,
854 Boulder, Colorado: Geological Society of America, 379, 63–81, https://doi.org/10.1130/0-8137-2379-5.63, 2004.
855 Joye, S. B. and Hollibaugh, J. T.: Influence of sulfide inhibition of nitrification on nitrogen regeneration in
856 sediments, Science, 270, 623–625, https://doi.org/10.1126/science.270.5236.62, 1995.
857 Kappler, A., Bryce, C., Mansor, M., Lueder, U., Byrne, J. M., and Swanner, E. D.: An evolving view on
858 biogeochemical cycling of iron, Nature Reviews Microbiology, 19, 360–374, https://doi.org/10.1038/s41579-020-
859 00502-7, 2021.
860 Klinkhammer, G. P.: Early diagenesis in sediments from the eastern equatorial Pacific, II. Pore water metal results,
861 Earth and Planetary Science Letters, 49, 81–101, https://doi.org/10.1016/0012-821X(80)90151-X, 1980.
862 Konhauser, K. O.: Introduction to geomicrobiology, John Wiley & Sons, 2009.
863 Kraal, P., Burton, E. D., and Bush, R. T.: Iron monosulfide accumulation and pyrite formation in eutrophic
864 estuarine sediments, Geochimica et Cosmochimica Acta, 122, 75–88, https://doi.org/10.1016/j.gca.2013.08.013,
865 2013.
866 Kraepiel, A. M., Chiffoleau, J.-F., Martin, J.-M., and Morel, F. M.: Geochemistry of trace metals in the Gironde
867 estuary, Geochimica et Cosmochimica Acta, 61, 1421–1436, https://doi.org/10.1016/S0016-7037(97)00016-1,
868 1997.
869 Learman, D. R., Voelker, B. M., Vazquez-Rodriguez, A. I., and Hansel, C. M.: Formation of manganese oxides
870 by bacterially generated superoxide, Nature Geoscience, 4, 95–98, https://doi.org/10.1038/ngeo1055, 2011.
871 Luther, G. W., Kostka, J. E., Church, T. M., Sulzberger, B., and Stumm, W.: Seasonal iron cycling in the salt-
872 marsh sedimentary environment: the importance of ligand complexes with Fe(II) and Fe(III) in the dissolution of
873 Fe(III) minerals and pyrite, respectively, Marine Chemistry, 40, 81–103, https://doi.org/10.1016/0304-
874 4203(92)90049-G, 1992.
875 Martin, J. B.: Nonconservative behavior of Br-/Cl- ratios during alteration of volcaniclastic sediments, Geochimica
876 et Cosmochimica Acta, 63, 383–391, https://doi.org/10.1016/S0016-7037(99)00036-8, 1999.
877 Martin, J. B., Cable, J. E., Swarzenski, P. W., and Lindenberg, M. K.: Enhanced submarine ground water discharge
878 from mixing of pore water and estuarine water, Groundwater, 42, 1000–1010, https://doi.org/10.1111/j.1745-
879 6584.2004.tb02639.x, 2004.

https://doi.org/10.5194/bg-2023-62
Preprint. Discussion started: 13 April 2023

880 McAllister, S. M., Barnett, J. M., Heiss, J. W., Findlay, A. J., MacDonald, D. J., Dow, C. L., Luther III, G. W.,
881 Michael, H. A., and Chan, C. S.: Dynamic hydrologic and biogeochemical processes drive microbially enhanced
882 iron and sulfur cycling within the intertidal mixing zone of a beach aquifer, Limnology and Oceanography, 60,
883 329–345, https://doi.org/10.1002/lno.10029, 2015.
884 McKew, B. A., Dumbrell, A. J., Taylor, J. D., McGenity, T. J., and Underwood, G. J.: Differences between aerobic
885 and anaerobic degradation of microphytobenthic biofilm-derived organic matter within intertidal sediments, FEMS
886 microbiology Ecology, 84, 495–509, https://doi.org/10.1111/1574-6941.12077, 2013.
887 Megonigal, J. P., Hines, M. E., and Visscher, P. T.: Anaerobic metabolism: linkages to trace gases and aerobic
888 processes, Biogeochemistry, 8, 317–424, https://doi.org/10.1016/B0-08-043751-6/08132-9, 2003.
889 Meiggs, D. and Taillefert, M.: The effect of riverine discharge on biogeochemical processes in estuarine sediments,
890 Limnology and Oceanography, 56, 1797–1810, https://doi.org/10.4319/lo.2011.56.5.1797, 2011.
891 Migeon, S., Weber, O., Faugeres, J.-C., and Saint-Paul, J.: SCOPIX: a new X-ray imaging system for core analysis,
892 Geo-Marine Letters, 18, 251–255, https://doi.org/10.1007/s003670050076, 1998.
893 Morelle, J., Roose-Amsaleg, C., and Laverman, A. M.: Microphytobenthos as a source of labile organic matter for
894 denitrifying microbes, Estuarine, Coastal and Shelf Science, 275, 108006,
895 https://doi.org/10.1016/j.ecss.2022.108006, 2022.
896 Mortimer, R. J., Harris, S. J., Krom, M. D., Freitag, T. E., Prosser, J. I., Barnes, J., Anschutz, P., Hayes, P. J., and
897 Davies, I. M.: Anoxic nitrification in marine sediments, Marine Ecology Progress Series, 276, 37–52,
898 https://doi.org/10.3354/meps276037, 2004.
899 Norman, L., Worms, I. A., Angles, E., Bowie, A. R., Nichols, C. M., Pham, A. N., Slaveykova, V. I., Townsend,
900 A. T., Waite, T. D., and Hassler, C. S.: The role of bacterial and algal exopolymeric substances in iron chemistry,
901 Marine Chemistry, 173, 148–161, https://doi.org/10.1016/j.marchem.2015.03.015, 2015.
902 Oldham, V. E., Siebecker, M. G., Jones, M. R., Mucci, A., Tebo, B. M., and Luther, G. W.: The Speciation and
903 Mobility of Mn and Fe in Estuarine Sediments, Aquatic Geochemistry, 25, 3–26, https://doi.org/10.1007/s10498-
904 019-09351-0, 2019.
905 O'Sullivan, L. A., Sass, A. M., Webster, G., Fry, J. C., Parkes, R. J., and Weightman, A. J.: Contrasting
906 relationships between biogeochemistry and prokaryotic diversity depth profiles along an estuarine sediment
907 gradient, FEMS microbiology ecology, 85, 143–157, https://doi.org/10.1111/1574-6941.12106, 2013.
908 Pace, A., Bourillot, R., Bouton, A., Vennin, E., Braissant, O., Dupraz, C., Duteil, T., Bundeleva, I., Patrier, P.,
909 Galaup, S., and Visscher, P. T.: Formation of stromatolite lamina at the interface of oxygenic–anoxygenic
910 photosynthesis, Geobiology, 16, 378–398, https://doi.org/10.1111/gbi.12281, 2018.
911 Pamatmat, M. M., Graf, G., Bengtsson, W., and Novak, C. S.: Heat production, ATP concentration and electron
912 transport activity of marine sediments, Mar. Ecol. Prog. Ser, 4, 135–144, https://doi.org/10.3354/meps004135,
913 1981.
914 Pereira, F.: Manganese-Tolerant Bacteria from the Estuarine Environment and Their Importance in Bioremediation
915 of Contaminated Estuarine Sites, in: Marine Pollution and Microbial Remediation, edited by: Naik, M. M. and
916 Dubey, S. K., Springer, Singapore, 153–175, https://doi.org/10.1007/978-981-10-1044-6_10, 2017.
917 Pitzer, K. S.: Theory, ion interaction approach, Activity coefficients in electrolyte solutions, 1, 157–208, 1979.
918 R Core Team: R: A language and environment for statistical computing, Vienna, Austria, 2013.

https://doi.org/10.5194/bg-2023-62
Preprint. Discussion started: 13 April 2023

Reasoner, D. J. and Geldreich, E. E.: A new medium for the enumeration and subculture of bacteria from potable water, Applied and Environmental Microbiology, 49, 1–7, https://doi.org/10.1128/aem.49.1.1-7.1985, 1985.

Relexans, J. C.: Measurement of the respiratory electron transport system (ETS) activity in marine sediments: state-of-the-art and interpretation. I. Methodology and review of literature data, Marine Ecology Progress Series, 136, 277–287, https://doi.org/10.3354/meps136277, 1996.

Revsbech, N. P., Madsen, B., and Jørgensen, B. B.: Oxygen production and consumption in sediments determined at high spatial resolution by computer simulation of oxygen microelectrode data, Limnol. Oceanogr, 31, 293–304, 1986.

Sagemann, J., Skowronek, F., Dahmke, A., and Schulz, H. D.: Pore-water response on seasonal environmental changes in intertidal sediments of the Weser Estuary, Germany, Environmental Geology, 27, 362–369, https://doi.org/10.1007/BF00766706, 1996.

Schwertmann, U. and Murad, E.: Effect of pH on the formation of goethite and hematite from ferrihydrite, Clays and Clay Minerals, 31, 277–284, https://doi.org/10.1346/CCMN.1983.0310405, 1983.

Sorensen, J. and Jorgensen, B. B.: Early diagenesis in sediments from Danish coastal waters: microbial activity and Mn-Fe-S geochemistry, Geochimica et Cosmochimica Acta, 51, 1583–1590, https://doi.org/10.1016/0016-7037(87)90339-5, 1987.

Sorensen, J., Tiedje, J. M., and Firestone, R. B.: Inhibition by sulfide of nitric and nitrous oxide reduction by denitrifying Pseudomonas fluorescens, Applied and Environmental Microbiology, 39, 105–108, https://doi.org/10.1128/aem.39.1.105-108.1980, 1980.

Stecko, J. P. and Bendell-Young, L. I.: Contrasting the geochemistry of suspended particulate matter and deposited sediments within an estuary, Applied Geochemistry, 15, 753–775, https://doi.org/10.1016/S0883-2927(99)00090-6, 2000.

Stumm, W. and Morgan, J. J.: An Introduction Emphasizing Chemical Equilibria in Natural Waters, Aquatic chemistry, 2, 178–184, 1996.

Sundby, B., Anderson, L. G., Hall, P. O., Iverfeldt, Å., van der Loeff, M. M. R., and Westerlund, S. F.: The effect of oxygen on release and uptake of cobalt, manganese, iron and phosphate at the sediment-water interface, Geochimica et Cosmochimica Acta, 50, 1281–1288, https://doi.org/10.1016/0016-7037(86)90411-4, 1986.

Thamdrup, B., Fossing, H., and Jørgensen, B. B.: Manganese, iron and sulfur cycling in a coastal marine sediment, Aarhus Bay, Denmark, Geochimica et Cosmochimica Acta, 58, 5115–5129, https://doi.org/10.1016/0016-7037(94)90298-4, 1994.

Thode-Andersen, S. and Jorgensen, B. B.: Sulfate reduction and the formation of 35S-labeled FeS, FeS2, and S0 in coastal marine sediments, Limnology and Oceanography, 34, 793–806, https://doi.org/10.4319/lo.1989.34.5.0793, 1989.

Thornton, D. C. O., Dong, L. F., Underwood, G. J. C., and Nedwell, D. B.: Factors affecting microphytobenthic biomass, species composition and production in the Colne Estuary (UK), Aquatic Microbial Ecology, 27, 285–300, https://doi.org/10.3354/ame027285, 2002.

Tugel, J. B., Hines, M. E., and Jones, G. E.: Microbial Iron Reduction by Enrichment Cultures Isolated from Estuarine Sediments, Applied and Environmental Microbiology, 52, 1167–1172, https://doi.org/10.1128/aem.52.5.1167-1172.1986, 1986.

https://doi.org/10.5194/bg-2023-62
Preprint. Discussion started: 13 April 2023

958 Underwood, G. and Kromkamp, J.: Primary Production by Phytoplankton and Microphytobenthos in Estuaries,
959 Advances in Ecological Research, Vol 29, 29, 93–153, https://doi.org/10.1016/S0065-2504(08)60192-0, 1999.
960 Underwood, G. J. and Paterson, D. M.: The importance of extracellular carbohydrate productionby marine epipelic
961 diatoms, Advances in botanical research, 40, 183–240, https://doi.org/10.1016/S0065-2296(05)40005-1, 2003.
962 Virolle, M.: Origine et prédiction spatio-temporelle des tapissages argileux dans les réservoirs silicoclastiques-
963 Apports de la comparaison entre des réservoirs enfouis (Permien et Crétacé) et un analogue actuel (estuaire de la
964 Gironde), PhD Thesis, Université Paris-Saclay, 537 pp., 2019.
965 Virolle, M., Féniès, H., Brigaud, B., Bourillot, R., Portier, E., Patrier, P., Beaufort, D., Jalon-Rojas, I., Derriennic,
966 H., and Miska, S.: Facies associations, detrital clay grain coats and mineralogical characterization of the Gironde
967 estuary tidal bars: A modern analogue for deeply buried estuarine sandstone reservoirs, Marine and Petroleum
968 Geology, 114, 104225, https://doi.org/10.1016/j.marpetgeo.2020.104225, 2020.
969 Virolle, M., Brigaud, B., Féniès, H., Bourillot, R., Portier, E., Patrier, P., Derriennic, H., and Beaufort, D.:
970 Preservation and distribution of detrital clay coats in a modern estuarine heterolithic point bar in the Gironde
971 estuary (Bordeaux, France), Journal of Sedimentary Research, 91, 812–832, https://doi.org/10.2110/jsr.2020.146,
972 2021.
973 Visscher, P. T. and van Gemerden, H.: Production and consumption of dimethylsulfoniopropionate in marine
974 microbial mats, Applied and Environmental Microbiology, 57, 3237–3242,
975 https://doi.org/10.1128/aem.57.11.3237-3242.1991, 1991.
976 Visscher, P. T. and Stolz, J. F.: Microbial mats as bioreactors: populations, processes, and products, in:
977 Geobiology: Objectives, Concepts, Perspectives, Elsevier, 87–100, 2005.
978 Visscher, P. T., Beukema, J., and van Gemerden, H.: In situ characterization of sediments: measurements of
979 oxygen and sulfide profiles with a novel combined needle electrode, Limnology and oceanography, 36, 1476–
980 1480, https://doi.org/10.4319/lo.1991.36.7.1476, 1991.
981 Visscher, P. T., Reid, R. P., and Bebout, B. M.: Microscale observations of sulfate reduction: Correlation of
982 microbial activity with lithified micritic laminae in modern marine stromatolites, Geology, 28, 919–922,
983 https://doi.org/10.1130/0091-7613(2000)28<919:MOOSRC>2.0.CO;2, 2000.
984 Widerlund, A. and Ingri, J.: Redox cycling of iron and manganese in sediments of the Kalix River estuary, Northern
985 Sweden, Aquatic Geochemistry, 2, 185–201, https://doi.org/10.1007/BF00121631, 1996.
986

https://doi.org/10.5194/bg-2023-62
Preprint. Discussion started: 13 April 2023

Captions:

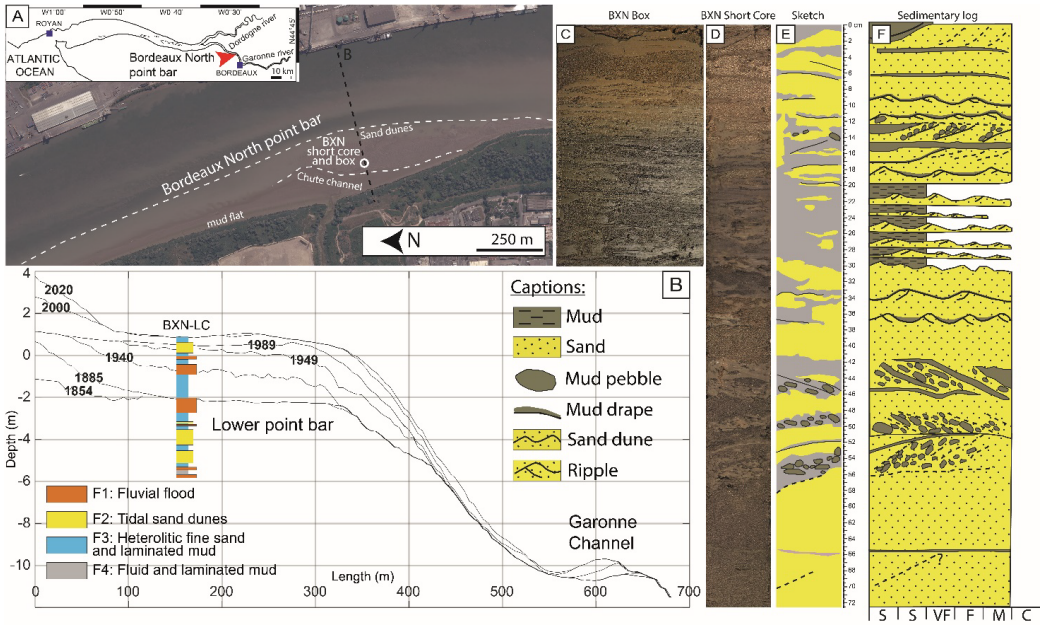

Figure 1: (A) Map of the Gironde estuary with location of the Bordeaux North point bar and satellite image of the point bar at low tide (© Google Earth Pro) showing the location of the studied cores (BXN-LC, BXN-SC and BXN-B) and surface biofilm samples. Three sedimentary domains are visible in the intertidal zone of the point bar: the mud flat, the chute channel (low energy), and the sand dunes (high energy). The dashed black line represents the cross section shown in part B. (B) Cross section of the Bordeaux North point bar based on bathymetric surveys by the Port de Bordeaux. Each black line represents the surface of the point bar for a given year. The top half of core BXN-LC was deposited between the second half of the 19th century and the 2000s. (C) Image of BXN-Box showing a change in sediment color from orange to grey at ca. 14 cm. The main facies is composed of small ripples alternating with clay drapes (wavy bedding) and is typical of an intertidal zone with moderate tidal currents. (D) Image, (E) mapping of sand vs. clay and (F) sedimentary log from BXN-SC. The top 30 centimeters of BXN-SC are similar to BXN-B, but the bottom 32 centimeters show high energy tidal dunes. In order to simplify the presentation of results, BXN-B and BXN-SC are merged into one synthetic core in the following figures.

https://doi.org/10.5194/bg-2023-62
Preprint. Discussion started: 13 April 2023

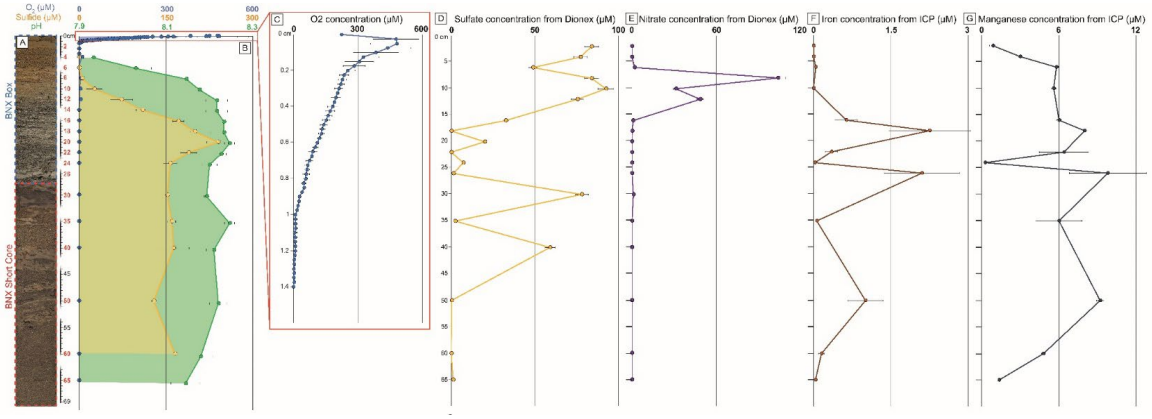

Figure 2: Porewater concentration profiles of major elements in BXN-B and BXN-SC in function of depth. (A) picture of BXN-B (circled in blue) merged with BXN-SC (circled in red). (B) Profiles of dissolved oxygen (in blue), sulfide (in yellow-orange) and pH (in green) measured using microelectrodes. (C) The red square highlighted a zoom in the upper 1.5 cm of the sediment to see detail of the oxygen profile. Profiles of sulfate (yellow, D) and nitrate (purple, E) concentrations measured by ion chromatography. Profiles of total dissolved iron (brown, F) and manganese (grey, G) measured by ICP-OES.

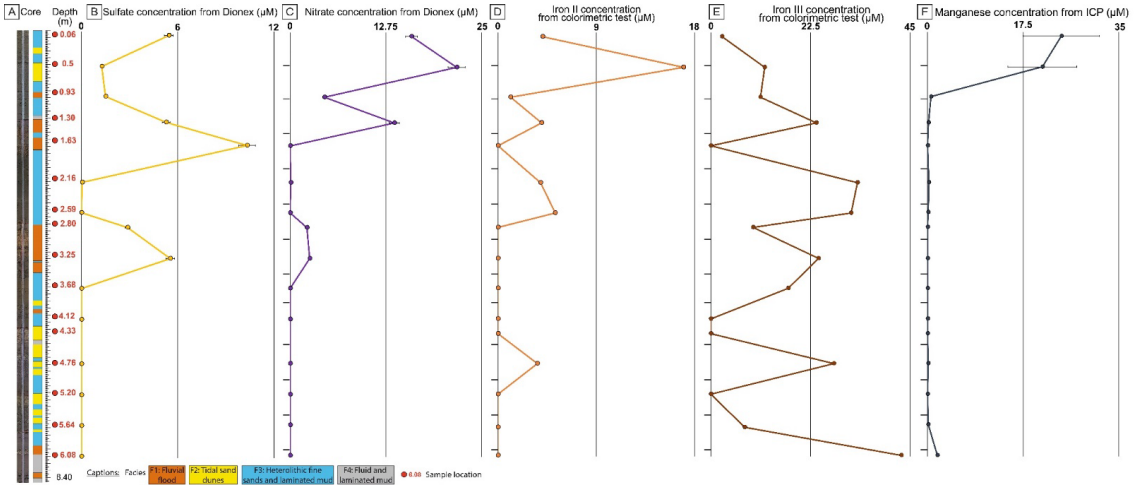

Figure 3: Porewater concentration profiles of major elements in BXN-LC in function of depth. (A) Picture and sedimentological interpretation of BXN-LC (see Duteil et al., 2022 for details). Sample locations are marked by red dots. Profiles of sulfate (B, yellow) and nitrate (C, purple) concentrations measured by ion chromatography. Profiles of species Fe II (D, orange) and Fe III (E, brown) measured by a colorimetric assay. Profile of manganese (F, grey) measured by ICP-OES.

https://doi.org/10.5194/bg-2023-62
Preprint. Discussion started: 13 April 2023

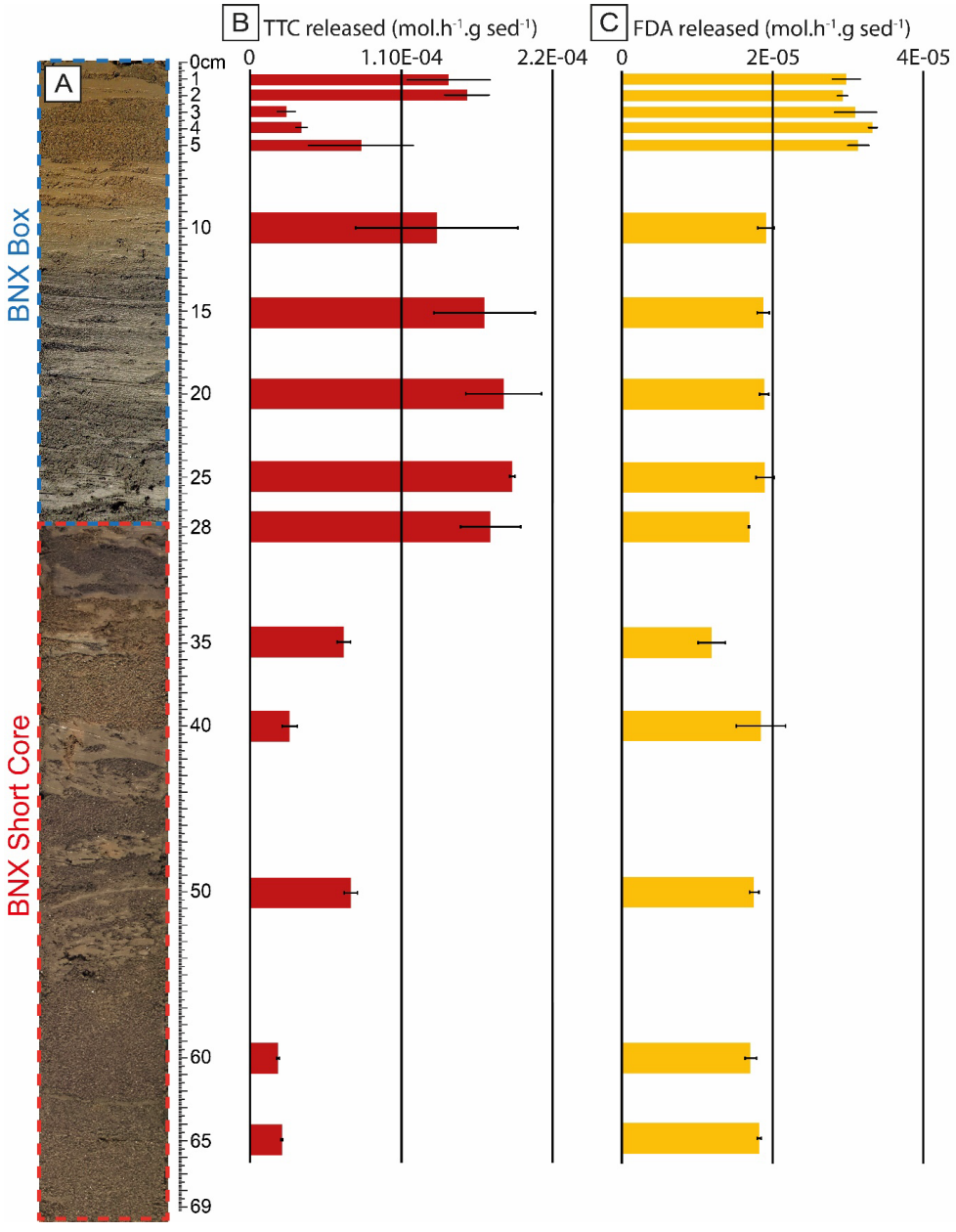

Figure 4: Profiles of metabolic and enzymatic activities in the sediment in BXN-B and BXN-SC. (A) picture of BXN-B (circled in blue) merged with BXN-SC (circled in red). The depth of the samples is indicated along the ruler. The rate TTC reduction (B, red) is a proxy for metabolic activity. The rate of hydrolyzed FDA (C, yellow) is a proxy for hydrolytic enzyme activity.

https://doi.org/10.5194/bg-2023-62
Preprint. Discussion started: 13 April 2023

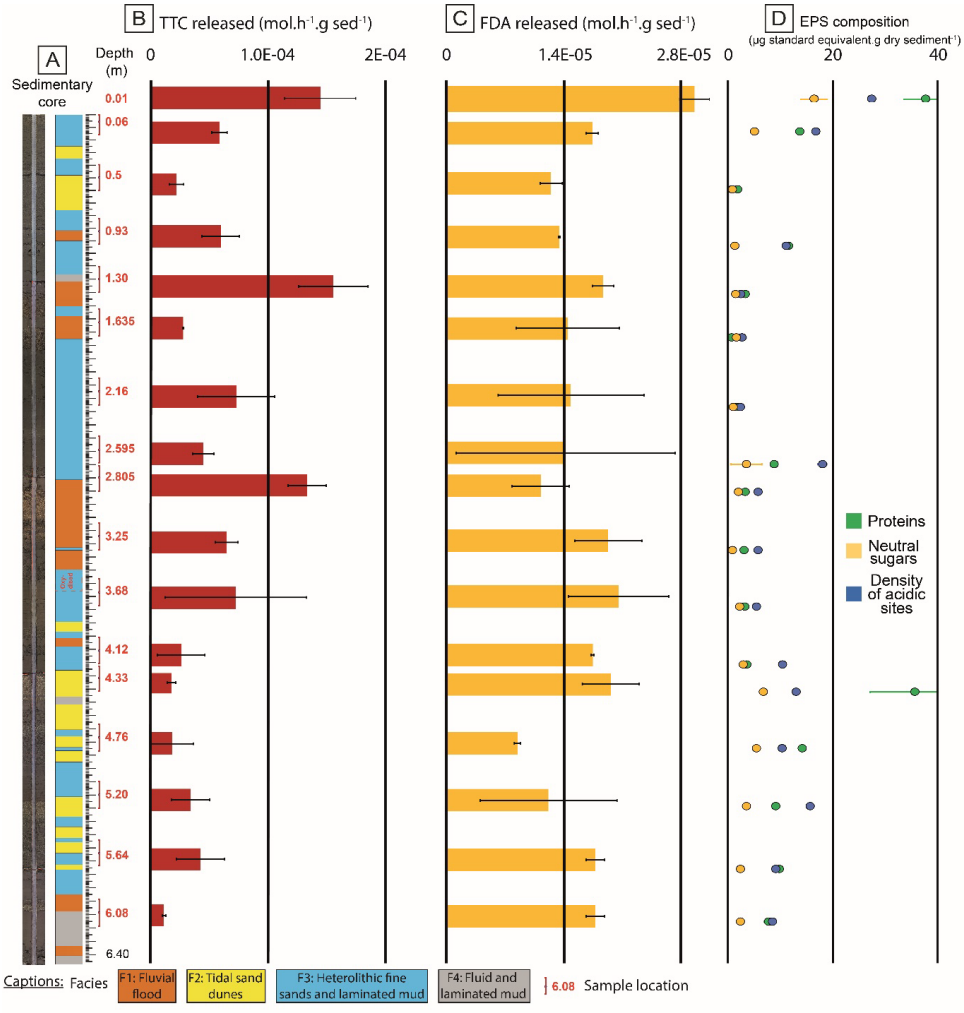

Figure 5: Profiles of metabolic and enzymatic activities in the sediment in BXN-LC. (A) Picture and sedimentological interpretation of BXN-LC. Sample locations are marked by red dots. The rate TTC reduction (B, red) is a proxy for metabolic activity. The rate of hydrolyzed FDA (C, yellow) is a proxy for hydrolytic enzymes activity. EPS physico-chemical properties adapted from Duteil et al., 2022 are plotted to the right (D): concentrations of neutral sugars (yellow), proteins (green) and density of acidic sites (blue).

https://doi.org/10.5194/bg-2023-62
Preprint. Discussion started: 13 April 2023

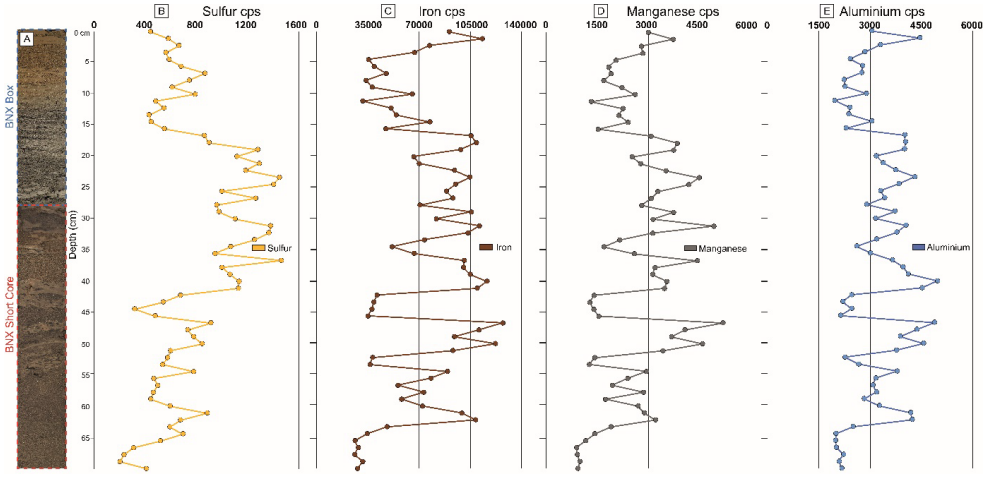

Figure 6: X-ray fluorescence spectrometric results of selected elements in BXN-B and BXN-SC. (A) picture of BXN-B (circled in blue) merged with BXN-SC (circled in red). Plot of: sulfur (B, yellow), iron (C, brown), manganese (D, grey) and aluminum (E, blue) measured by core-scale XRF on BXN-B and BXN-SC.

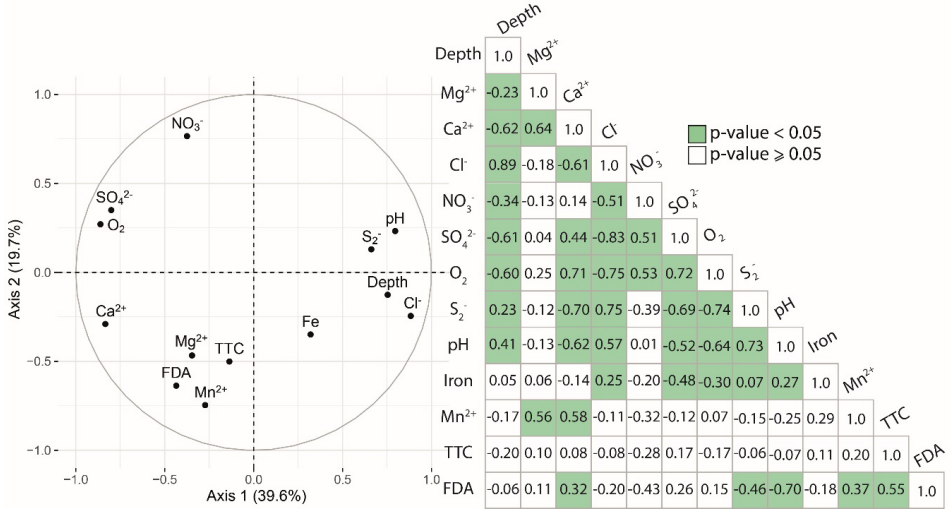

	Depth	Mg^{2+}	Ca^{2+}	Cl^-	NO_3^-	SO_4^{2-}	O_2	S_2^-	pH	Iron	Mn^{2+}	TTC	FDA
Depth	1.0												
Mg^{2+}	-0.23	1.0											
Ca^{2+}	-0.62	0.64	1.0										
Cl^-	0.89	-0.18	-0.61	1.0									
NO_3^-	-0.34	-0.13	0.14	-0.51	1.0								
SO_4^{2-}	-0.61	0.04	0.44	-0.83	0.51	1.0							
O_2	-0.60	0.25	0.71	-0.75	0.53	0.72	1.0						
S_2^-	0.23	-0.12	-0.70	0.75	-0.39	-0.69	-0.74	1.0					
pH	0.41	-0.13	-0.62	0.57	0.01	-0.52	-0.64	0.73	1.0				
Iron	0.05	0.06	-0.14	0.25	-0.20	-0.48	-0.30	0.07	0.27	1.0			
Mn^{2+}	-0.17	0.56	0.58	-0.11	-0.32	-0.12	0.07	-0.15	-0.25	0.29	1.0		
TTC	-0.20	0.10	0.08	-0.08	-0.28	0.17	-0.17	-0.06	-0.07	0.11	0.20	1.0	
FDA	-0.06	0.11	0.32	-0.20	-0.43	0.26	0.15	-0.46	-0.70	-0.18	0.37	0.55	1.0

Figure 7: Principal Components Analysis (PCA) of the BXN-B and BXN-SC data. Left part, PCA correlation circle plot of variables of the porewater composition in BXN-B and BXN-SC. Right part, correlation matrix of Pearson's r coefficients between depth, concentration of the main dissolved elements, oxygen and pH for the 18 samples. Green boxes indicate a p-value <0.05.

https://doi.org/10.5194/bg-2023-62
Preprint. Discussion started: 13 April 2023

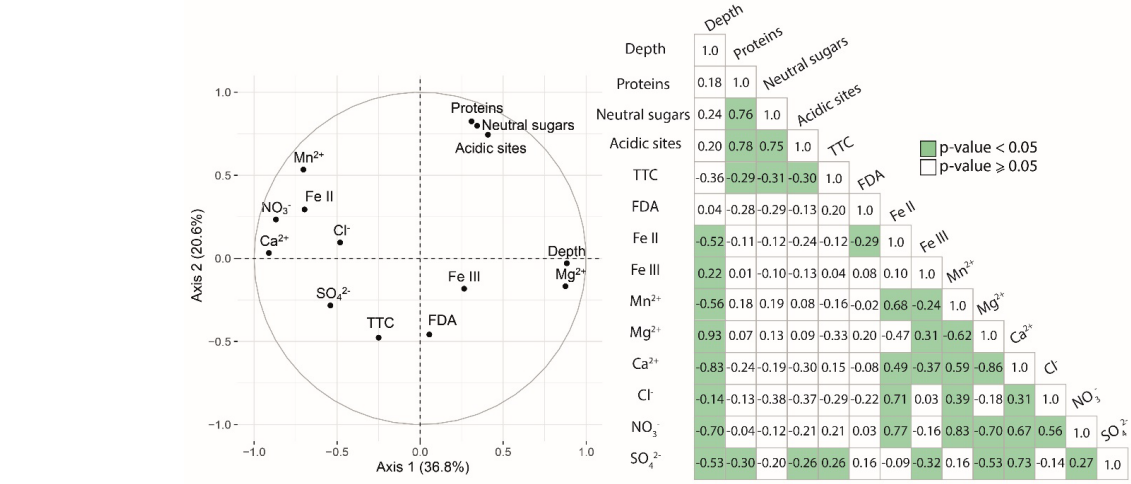

	Depth	Proteins	Neutral sugars	Acidic sites	TTC	FDA	Fe II	Fe III	Mn^{2+}	Mg^{2+}	Ca^{2+}	Cl^-	NO_3^-	SO_4^{2-}
Depth	1.0													
Proteins	0.18	1.0												
Neutral sugars	0.24	0.76	1.0											
Acidic sites	0.20	0.78	0.75	1.0										
TTC	-0.36	-0.29	-0.31	-0.30	1.0									
FDA	0.04	-0.28	-0.29	-0.13	0.20	1.0								
Fe II	-0.52	-0.11	-0.12	-0.24	-0.12	-0.29	1.0							
Fe III	0.22	0.01	-0.10	-0.13	0.04	0.08	0.10	1.0						
Mn^{2+}	-0.56	0.18	0.19	0.08	-0.16	-0.02	0.68	-0.24	1.0					
Mg^{2+}	0.93	0.07	0.13	0.09	-0.33	0.20	-0.47	0.31	-0.62	1.0				
Ca^{2+}	-0.83	-0.24	-0.19	-0.30	0.15	-0.08	0.49	-0.37	0.59	-0.86	1.0			
Cl^-	-0.14	-0.13	-0.38	-0.37	-0.29	-0.22	0.71	0.03	0.39	-0.18	0.31	1.0		
NO_3^-	-0.70	-0.04	-0.12	-0.21	0.21	0.03	0.77	-0.16	0.83	-0.70	0.67	0.56	1.0	
SO_4^{2-}	-0.53	-0.30	-0.20	-0.26	0.26	0.16	-0.09	-0.32	0.16	-0.53	0.73	-0.14	0.27	1.0

Figure 8: Principal Components Analysis (PCA) of the BXN-LC data. Left part, PCA correlation circle plot of variables of the porewater composition in BXN-LC. Right part, correlation matrix of Pearson's r coefficients between depth, concentration of the main dissolved elements for the 16 samples. Green boxes indicate p-value <0.05.

https://doi.org/10.5194/bg-2023-62
Preprint. Discussion started: 13 April 2023

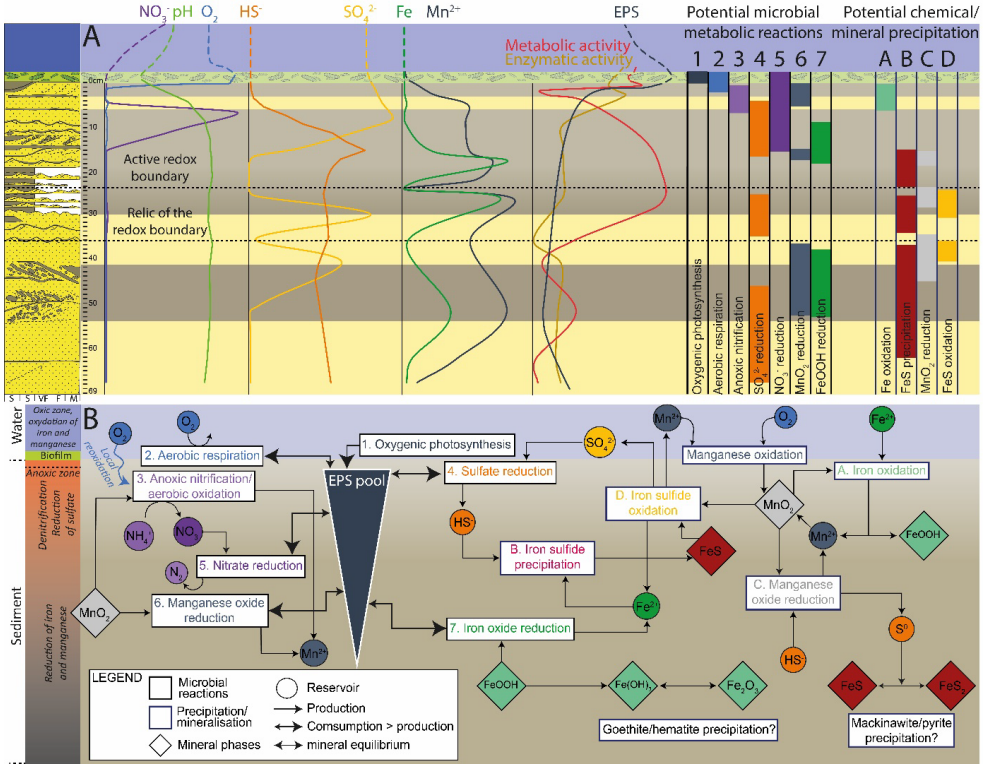

Figure 9: Schematic conceptual model of the potential relationships between geochemical gradients, microbial activity, exopolymeric substances, and their impact on early diagenesis in estuarine sediments. The predicted change in the concentration of the major dissolved elements in the water column above the sediments is depicted by a dotted line. Microbial metabolic reactions are indicated with numbers and diagenetic processes by letters. (A; top panel) To the left, sedimentary description of BXN-B and BXN-SC. The size of the diatom biofilm has been deliberately exaggerated to visualize its impact on the environment at the surface sediment. The profiles show the evolution of porewater composition (ions, oxygen and pH), microbial and enzymatic activities and EPS concentration (adapted from Duteil et al., 2022). To the right, the potential depth range of metabolic reactions, as well as of chemical/mineral precipitation, are indicated by color bars. (B; bottom panel) To the left, description of the main geomicrobiological zones in the sediment related to the main metabolisms. On the right, geomicrobiological model showing potential interactions between microbial metabolisms and mineral precipitation/dissolution. Metabolic reactions are referenced by numbers, while precipitation reactions are referenced by letters. The color is the same for one compound in the two panels e.g., purple for nitrates.

https://doi.org/10.5194/bg-2023-62
Preprint. Discussion started: 13 April 2023

Depth (cm)	mu	Lag	Q	CFU 30
6	0.166	0	5.42	$5.3.10^8$
50	0.24	3.57	4.21	$2.8.10^7$
93	0.133	0	2.61	$5.3.10^8$

Table 1: Measurements of microbial activity with isothermal calorimetry (IMC). These measurements were performed on sediments from three depths in BXN-LC. Mu corresponds to the growth rate, i.e., how fast the bacterial community can grow using the substrate. Lag is the time before the bacterial community is active (negative value = 0). Total heat Q is the total heat released during the experiment, maxHF is the peak of thermal activity and CFU 30 the counting of bacterial colonies after 30 days of culture.

BNX-B and BXN-SC	Saturation index					
Depth	Ferrihydrite	Goethite	Hematite	Calcite	Mackinawite	Pyrite
cm	$Fe(OH)_3$	FeO(OH)	Fe_2O_3	$CaCO_3$	FeS	FeS_2
2	-5.19	0.41	2.78	0.08	-2.82	2.53
4	-5.32	0.28	2.52	0.09	-2.96	2.42
6	-5.72	-0.13	1.72	0	-3.44	1.76
10	-5.47	0.13	2.22	0.39	1.03	9.03
16	-5.87	-0.27	1.43	0.07	1.59	10.05
18	-5.44	0.15	2.28	0.03	2.09	10.57
22	-6.25	-0.65	0.67	0.28	1.3	9.68
24	-7.35	-1.75	-1.53	0.03	0.18	8.47
26	-5.43	0.17	2.31	0.23	2.15	10.21
35	-6.94	-1.34	-0.71	-0.49	0.62	8.76
50	-5.72	-0.12	1.73	0.09	1.88	9.69
60	-6.77	-1.18	-0.38	0.09	0.93	8.98
65	-6.49	-0.89	0.19	0.03	0.43	8.07

Table 2: Saturation indices of some mineral phases in BXN-B and BXN-SC according to the modeling performed with phreeQc.

https://doi.org/10.5194/bg-2023-62
Preprint. Discussion started: 13 April 2023

BXN-LC	Saturation index						
Depth	Ferrihydrite	Goethite	Hematite	Siderite	Calcite	Dolomite	Aragonite
cm	$Fe(OH)_3$	FeO(OH)	Fe_2O_3	$FeCO_3$	$CaCO_3$	$CaMg(CO_3)_2$	$CaCO_3$
6	2.5	8.09	18.16	0.21	0.26	0.26	0.11
50	3.17	8.77	19.52	0.91	0.39	0.72	0.25
93	3.14	8.74	19.45	-0.41	0.02	0.15	-0.12
130	3.47	9.07	20.11	0.28	0.29	0.74	0.15
163	1.65	7.25	16.47	-0.99	0.55	1.08	0.41
216	3.61	9.21	20.39	0.21	0.04	0.42	-0.1
259	3.59	9.19	20.35	0.39	0.09	0.56	-0.05
280	3.07	8.67	19.31	-1.05	0.15	0.62	0.01
325	3.48	9.08	20.13	-0.98	0.13	0.83	-0.02
368	3.34	8.93	19.84	-0.96	0.16	0.92	0.02
412	1.65	7.25	16.47	-0.94	0.06	0.86	-0.08
476	3.54	9.13	20.24	0.4	0.17	1.04	0.03
520	1.65	7.25	16.47	-0.92	0.2	0.97	0.06
564	2.98	8.58	19.13	-0.89	0.22	1.12	0.07
608	3.73	9.33	20.62	-0.94	0.04	0.8	-0.1

Table 3: Saturation indices of some mineral phases in BXN-LC according to the modeling performed with phreeQc.